NUMERICAL MODELLING OF SUBGLACIAL EROSION AND SEDIMENT TRANSPORT AND ITS APPLICATION TO THE NORTH AMERICAN ICE SHEETS OVER THE LAST GLACIAL CYCLE

ALEXANDRE MELANSON

Numerical Modelling of Subglacial Erosion and Sediment Transport and its Application to the North American Ice Sheets over the Last Glacial Cycle

by

©Alexandre Melanson

A thesis submitted to the School of Graduate Studies in partial fulfillment of the requirements for the degree of

Master of Science

Department of Physics and Physical Oceanography

Memorial University of Newfoundland

July 2012

St. John's Newfoundland

Abstract

Present-day sediment distribution offers a potentially strong constraint on past ice sheet evolution, however, glacial system models (GSMs) cannot address this while lacking proper representations of subglacial sediment production and transport. Toward this goal, I present a continental subglacial process model for sediment production, entrainment, transport, and deposition. The model is driven by the data-calibrated MUN 3-D GSM and by a newly developed subglacial hydrology component. Model results are compared against the present-day distribution of glacigenic sediment over North America and geological estimates of Laurentide erosion. Given the model's parametric sensitivity, the calculated erosion depths fall within the geological estimates of Laurentide erosion, with the exception of Hallet's abrasion law that underestimates abrasion by at least an order of magnitude. In, addition, the model overestimates sediment entrainment and thus englacial transport, which either suggests that the large-scale representation of regelation intrusion is inadequate or that the basal hydrology module underestimates water pressures.

Acknowledgements

I sincerely thank my supervisors, Dr. Lev Tarasov and Dr. Trevor Bell for giving me the opportunity to work on this project and for offering their valuable insight and guidance throughout the course of my program. Special thanks to my colleagues Robert Briggs and Mark Kavanagh for offering, on several occasion, much appreciated practical assistance, as well as to the rest of the MUN Glacial System Dynamics group, Tristan Hauser, Kevin Le Morzadec and Taimaz Bahadory for their continued moral support. Funding from the Natural Sciences and Engineering Research Council of Canada (NSERC) and the School of Graduate Studies is gratefully acknowledged.

Table of Contents

List of Tables

List of Figures

List of Acronyms

BP	Before Present
GSM	Glacial System Model
HB	Hudson Bay
IRD	Ice Rafted Debris
JB	James Bay
LGM	Last Glacial Maximum
LIS	Laurentide Ice Sheet
MA	Manitoba
ND	North Dakota
OH	Ohio
ON	Ontario
SD	South Dakota

List of Symbols

Symbol	Description	Units
$\dot{A}$	Abrasion rate	m s^{-1}
A_e	Effective area of contact	m^2
A_r	Cross sectional area of the abrading particle	m^2
B_g	Thermally activated Glen flow law coefficient	s^{-1} Pa^{-3}
$\dot{b}_{melt}$	Basal melting rate	m s^{-1}
c	Sediment cohesion	Pa
C	Englacial sediment concentration by volume	-
C_b	Basal debris concentration	m^{-2}
$C^\star_{crit}$	Critical englacial sediment concentration by volume	-
$C^\star_{emp}$	Scaling factor for the empirical erosion law	Pa^{-1}
$C^\star_{max}$	Maximum englacial sediment concentration by volume	-
$C^\star_{quar}$	Quarrying scaling factor	Pa^{-1}
D	Diffusion coefficient for vertical mixing	m^2 s^{-1}
$\tilde{D}^\star$	Diffusion coefficient prefactor	m^2 s^{-1}
D_o	Newtonian sediment reference deformation rate	s^{-1}
$\dot{E}$	Erosion rate	m s^{-1}
$\dot{E}_{emp}$	Erosion rate for the empirical law	m s^{-1}

Symbol	**Description**	**Units**
f_{bed}^{N}	Normal bed modification factor	-
f_{bed}^{T}	Tangential bed modification factor	-
F_N	Normal contact force	N
g	Gravitational acceleration	$\mathrm{m\ s^{-2}}$
H_b	Thickness of the modelled basal ice	m
$h_c^\star$	Sediment saturation thickness	m
$h_f^\star$	Water film thickness	m
$h_{max}^\star$	Maximum initial sediment thickness	m
h_{sed}	Sediment thickness	m
$\tilde{h}_{sed}^\star$	Shielding factor	m
$HV^\star$	Bedrock hardness	Pa
h_w	Effective subglacial water thickness	m
k_{abr}	Abrasion wear coefficient	-
K_s	Apparent conductivity of the sediment	$\mathrm{m^2\ Pa^{-1}\ s^{-1}}$
K_w	Hydraulic conductivity of the sediment	$\mathrm{m\ s^{-1}}$
k_z	Vertical grid cell identifier	-
l_a	Entrained array depth	m
L_{fus}	Latent heat of fusion of ice	$\mathrm{J\ kg^{-1}}$
$l_{max}^\star$	Cut-off englacial array thickness	m
l_{mod}	Array depth modifier	-
$n_s^\star$	Sediment rheology exponent	-
$n_p^\star$	Residual pressure exponent for quarrying	-

Symbol	Description	Units
$N_z^\star$	Number of vertical cells	-
P_e	Effective normal pressure	Pa
P_i	Ice overburden pressure	Pa
P_m	Pressure melting coefficient	K Pa^{-1}
$\tilde{P}_r$	Typical value for the residual pressure	Pa
P_s	Separation pressure	Pa
P_w	Basal water pressure	Pa
$\dot{Q}$	Quarrying rate	m s^{-1}
$\vec{Q}_s$	Sediment deformation flux	m^2 s^{-1}
$\vec{Q}_w$	Horizontal water flux	m^2 s^{-1}
R	Abrading particle radius	m
$\tilde{R}$	Transition radius	m
$R^\star_{mean}$	Mean of the grain-size distribution	m
S_w	Basal water mass balance	m s^{-1}
t	Time coordinate	s
$\vec{v}_i$	Horizontal ice velocity	m s^{-1}
$v^\star_{max}$	Maximum entrainment rate	m s^{-1}
$\dot{V}_{mix}$	Vertical mixing coefficient	s^{-1}
v_n	Normal ice velocity	m s^{-1}
$\dot{V}_{net}$	Net entrainment/deposition rate	m s^{-1}
v_{par}	Abrading particle's absolute velocity	m s^{-1}
v_r	Entrainment rate	m s^{-1}

Symbol	Description	Units
v_s	Sliding velocity	m s^{-1}
$\tilde{v}_s$	Typical sliding velocity	m s^{-1}
v_{sed}	Horizontal velocity within the sediment	m s^{-1}
z	Vertical distance from the ice/bed interface	m
$\tilde{z}^\star$	Attenuation factor for the z-dependence of vertical mixing	m
z_b	Bed elevation	m
z_d	Sediment deformation depth	m
$Z_r^\star$	Thermal resistivity of englacial material	m K W^{-1}
Δz	Grid cell thickness	m
η	Effective ice viscosity	Pa s
$\mu^\star$	Rock-rock friction coefficient	-
$\mu_o^\star$	Newtonian sediment reference viscosity	Pa s
$\varphi^\star$	Sediment angle of internal friction	-
ρ_i	Density of ice	kg m^{-3}
ρ_s	Sediment density	kg m^{-3}
ρ_w	Water density	kg m^{-3}
τ_b	Basal shear stress	Pa
τ_{sed}	Shear stress within the sediment	Pa
$\zeta^\star$	Basal roughness	-

Chapter 1

Introduction and Overview

1.1 Motivations

As primary products of ice-bed interactions, glacial erosional and depositional landforms offer a potentially strong constraint on past ice sheet evolution. The great North American ice sheets, for instance, have been the subject of extensive palaeoglaciological reconstructions based on glacial geomorphic data (Benn and Evans, 2010). More precisely, past glacial conditions, such as ice thickness, extent and flow pattern, are inferred from subglacial bedforms, till characteristics, and moraine positions, and are temporally constrained by geochronological data. This type of inversion modelling is based on genetic classifications of sediment-landform associations and is, therefore, dependent on field interpretations of glacial landforms and deposits. A further challenge is introduced by the palimpsest nature of glacial landscapes, which generally limits interpretations to the late Pleistocene.

Over the course of the last few decades, numerical glacial system models (GSMs) have emerged as an alternative approach for reconstructing palaeo ice sheets. Their advantage over inversion models stems from their ability to quantitatively compare their results to various types of field observation and to provide spatial and temporal coverage even in the absence of constraint data. In their current state, GSM results are comparable with geophysical observations, such as relative sea-level data and present-day rates of surface uplift. The use of geomorphic data is, however, limited to constraining marine and terrestrial limits based on ice marginal features, as well as ice flow pattern based on directional erosional and depositional landforms. Because GSMs lack proper representations of subglacial erosion and sediment transport processes, they cannot fully predict the geomorphic and geologic outcomes of glaciations. Incorporating such basal process components in GSMs is thus a necessary step toward exploiting the broader range of glacial geomorphological observations for constraint purposes.

This thesis addresses this research gap by developing a continental-scale subglacial process model that accounts for sediment production, entrainment, transport, and deposition (hereafter referred to as the *sediment model*). This model is applied to the North American ice sheets over the last glacial cycle and predicts the distribution of glacigenic sediment and cumulative erosion patterns. These results are compared against the present-day sediment cover over North America and geological estimates of Laurentide erosion. Although the processes of sediment production, entrainment, transport and deposition have been to some degree addressed theoretically, few attempts have been made to implement them in continental-scale GSMs, the most recent of which was the work of Hildes (2001;2004). This thesis is thus a continuation of his attempt to develop a coupled basal process/ice sheet model.

Hildes (2001; 2004) adopted a process-oriented approach where distinct erosional and transport mechanisms were physically modelled based on existing theoretical descriptions of these processes. This contrasts with the use of empirical laws more commonly implemented in GSMs (see Section 2.2.3.2). This process-oriented approach was combined with a lithological description of the bed to represent subglacial processes on the continental-scale. This method allowed the trajectory of specific lithologies to be predicted, thus the extent and composition of modelled glacial deposits were compared against those of observed dispersal trains. Although I do not include sub-grid lithological information, I do adopt several of Hildes' approaches, including the use of Hallet's abrasion law (Hallet, 1979b) and Philip's law for regelation intrusion (Philip, 1980), and the representation of vertical and horizontal englacial transport by variations in debris concentration. In addition, I present a novel quarrying law based on the estimated extent of subglacial cavities, implement Boulton's analysis of abrasion (Boulton, 1979) for comparison with that of Hallet, and add a soft-bed deformation component based on the model of Jenson (1995). These aspects are discussed in detail in Section 2.2

1.2 Objectives and approach

The primary goal of this thesis is to develop a continental-scale subglacial erosion and sediment transport model consistent with geological estimates of cumulative erosion and with the observed pattern of glacigenic deposits over North America. In addition, I address the following key questions:

- Can process-oriented erosion laws be replaced by simple empirical relationships between erosion rate and some glaciological variable?

- When implemented in GSMs, do Hallet's and Boulton's abrasion laws produce comparable erosion patterns?
- Can a large-scale quarrying law based on the extent of subglacial cavities produce realistic erosion patterns?
- Which of subglacial deformation and englacial transport was the most efficient transport mechanism of the North American ice sheets?

To properly address these questions, the results presented in this thesis are obtained in the context of a sensitivity analysis. As discussed in Section 2.2.1, this approach consists in defining realistic ranges for the poorly constrained parameters used in the sediment model and in systematically generating the associated ranges of model outcomes. This approach is superior to using a single set of parameter values because it allows the parametric sensitivity of the model to be examined and the importance of different processes and variables to be identified. Systematic sensitivity analyses, as well as attempts to address the questions outlined above in the continental-scale context, have so far been lacking in this line of research.

Furthermore, when conducting modelling studies that involve several different topics, such as the variety of subglacial processes implemented in the sediment model, it is tempting to present the entire range of possible results that can be generated by the model, regardless of their relevance or their compatibility with physical observations. Such an approach would yield a very detailed documentation of the model's behaviour, but would be at risks of being a purely numerical modelling exercise with limited scope. In the hope of presenting a study that has value to the ice sheet modelling community, I attempt to avoid this approach by presenting results that can, in general, be compared to available data or to other models, and by addressing glaciologically relevant topics in most of the discussions.

1.3 Structure

This thesis is written in manuscript format (in contrast to traditional format), as such, its content is presented in the style of journal articles and will be prepared for publication. In this case, the supervisory committee agreed that a single manuscript was preferable given the nature and scope of the research undertaken. This manuscript is presented in Chapter 2 and is written as a stand-alone research paper, it thus contains some background material that is repeated from this introductory chapter. Chapter 3 consists of summary comments and descriptions of potential future research directions resulting from this thesis. The bibliography serves for the whole thesis.

1.4 Co-authorship statement

Authorship for the paper presented in Chapter 2 is in the following order: Mr. Alexandre Melanson (thesis author), Dr. Trevor Bell (thesis co-supervisor), and Dr. Lev Tarasov (thesis supervisor). Dr. Bell is a Professor with the Department of Geography of Memorial University of Newfoundland, and Dr. Tarasov is an Associate Professor with the Department of Physics and Physical Oceanography of Memorial University of Newfoundland.

Dr. Tarasov developed the initial idea and direction of the project, after which Mr. Melanson conceptualized the detailed form and structure of the model presented here. Mr. Melanson subsequently wrote the code for the model and performed the numerical simulations as well the data analysis. Related models were provided by Dr. Tarasov

(MUN 3-D GSM, as well as the calibrated set of GSM parameters) and by Mr. Mark Kavanagh (basal hydrology solver), a Master's student of Dr. Tarasov. Dr. Bell provided supervisory guidance and key knowledge pertaining to glacial geomorphology.

The research paper presented in Chapter 2 was written entirely by Mr. Melanson, with the exception of Section 2.2.6 that was provided by Dr. Tarasov. Dr. Bell and Dr. Tarasov thoroughly reviewed the manuscript and suggested minor revisions.

Chapter 2

Numerical Modelling of Subglacial Erosion and Sediment Transport and its Application to the North American Ice Sheets over the Last Glacial Cycle

Abstract

Present-day sediment distribution offers a potentially strong constraint on past ice sheet evolution, however, glacial system models (GSMs) cannot address this while lacking proper representations of subglacial sediment production and transport. Incorporating these elements in GSMs is also required in order to quantify the impact of changing sediment cover on glacial cycle dynamics.

Toward this goal, I present a subglacial process model (hereafter referred to as the *sediment model*) that incorporates mechanisms for sediment production, entrainment, transport, and deposition. Bedrock erosion is calculated either by Hallet's or Boulton's abrasion law, and by a novel quarrying law parameterized as a function of subglacial cavity extent. These process-oriented eroison laws are compared against a simple empirical relationship between erosion rate and the work done by basal stress. Sediment entrainment is represented by Philip's law for regelation intrusion and soft-bed deformation is included as a subglacial sediment transport mechanism, the rheology of which is assumed to be weakly non-linear. The model is driven by the data-calibrated MUN 3-D GSM and a newly developed subglacial hydrology module.

The sediment model is applied to the last North American glaciation and predicts sediment thickness and cumulative erosion patterns. These output fields are compared against the present-day glacigenic sediment distribution and geological estimates of Laurentide erosion. Given plausible parameter ranges for the sediment model (chosen a priori based on available literature or on heuristic arguments), the calculated erosion depths fall within the geological estimates of Laurentide erosion, with the exception of Hallet's abrasion law that underestimates abrasion by at least an order of magnitude. In addition, most of runs in the sensitivity set produce unrealistically thick and continuous moraines along the eastern, southern and western margins of the North American ice complex, which suggests that the model overestimates sediment entrainment and thus englacial transport. This is either explained by the misrepresentation of large-scale regelation intrusion or by underestimated basal water pressures. A realistic sediment distribution is only obtained when the entrainment rate is capped at the average basal melting rate, which suggests that a realistic balance between entrainment and deposition is achieved when the entrainment and basal melting rates are of the same order of magnitude.

2.1 Introduction

As first hand evidence of ice-bed interactions, glacial erosional and depositional landforms offer a potentially strong constraint on past ice sheet evolution. Although they are the primary tools used in qualitative reconstruction of paleo ice sheets (Glasser and Bennett, 2004), numerical modelling of the subglacial processes that created them has been hampered by the lack of direct observations of the ice/bed interface. However, the advent of new subglacial monitoring techniques has increased the accessibility of contemporary glacier beds (Benn and Evans, 2010) and, in conjunction with key laboratory experiments (Iverson, 1990; Kamb, 1991; Iverson, 1993; Iverson and Semmens, 1995; Tulaczyk et al., 2000; Byers et al., 2012), has allowed models to be formulated and validated against the new data. This has progressively allowed glacial system models (GSMs) to incorporate quantitative representations of subglacial erosional and transport processes (e.g. Alley and MacAyeal, 1994; Jenson et al., 1995; Egholm et al., 2012), although only few attempts have been made in the continental-scale context (Tulley, 1995; Hildes, 2001; Hildes et al., 2004; Jamieson et al., 2008, 2010).

Indeed, the majority of continental-scale GSMs still lack such representations and hence cannot predict the geologic and geomorphic outcomes of glaciations. This deficiency precludes them from fully exploiting the broad range of geomorphic data for constraint purposes. In addition, a subglacial process model fully coupled with ice dynamics calculations is necessary to properly address the impact of soft-bed deformation on ice sheet behaviour. This would be superior to the current practice of prescribing potential enhanced flow areas based on present-day sediment cover (e.g. Tarasov and Peltier, 2004).

Toward these goals, I present a continental-scale subglacial process model that accounts for sediment production, entrainment, transport, and deposition. The model is applied to the North American ice sheets over the last glacial cycle and predicts the distribution of glacigenic sediment and cumulative erosion patterns. This effort is a continuation of the work of Hildes (2001; 2004), who combined a process-oriented approach with a lithological description of the bed to represent these processes on the continental-scale. This method allowed the trajectory of specific lithologies to be predicted, thus the extent and composition of modelled glacial deposits was compared against that of observed dispersal trains. Although I do not include sub-grid lithological information, I do adopt several of Hildes' approaches, including the use of Hallet's abrasion law (Hallet, 1979b) and Philip's law for regelation intrusion (Philip, 1980), and the representation of vertical and horizontal englacial transport by variations in debris concentration. In addition, I present a novel quarrying law based on the estimated extent of subglacial cavities, implement Boulton's analysis of abrasion (Boulton, 1979) for comparison with that of Hallet, and add a soft-bed deformation component based on the model of Jenson (1995). The latter is included to assess the transport potential of subglacial deformation relative to englacial transport, and to determine whether it has an impact on the erosion pattern.

Moreover, I tackle the important question of whether continental-scale subglacial erosion models require the use of a process-oriented approach (where abrasion and quarrying are modelled separately with their own set of controlling variables), or can be simply reduced to an empirically-based scaling relationship between erosion rates and some glaciological variables (e.g. ice thickness, sliding velocity, etc.). Although both approaches have been applied to the continental-scale (see Section 2.2.3), there has been no attempt to compare and evaluate them. I thus specifically attempt to fill this research gap by implementing both approaches in the model and comparing them systematically. By adopting this goal, I implicitly oppose the notion that physically-based approaches should automatically be deemed superior. Rather, I support that there is no a priori reason to reject empirical laws, especially in the large-scale context, where it is conceivable that the small-scale variability of subglacial processes averages-out and thereby reveals a larger pattern controlled by the average value of glaciological variables.

Most of the results presented here were obtained in the context of a sensitivity analysis (see Section 2.2.1). This approach allows the sediment model's parametric sensitivity to be examined and the influence of different processes and variables (e.g. entrainment, sediment deformation, basal water pressure, etc.) on the predicted pattern of erosion and deposition to be identified. This approach, as well as attempts to address the question outlined above in the continental-scale context, have so far been lacking in this line of research.

2.2 Model description

I present below a two-component model that quantifies processes of subglacial sediment production, entrainment, transport and deposition. The *subglacial* component (2-D) acquires sediment from eroded bedrock and from melting of debris-laden ice, and transports it horizontally by soft-bed deformation. Where entrainment s, it yields material to the *englacial* component (3-D), which allows vertical and horizontal englacial transport of debris, and sediment deposition in zones of dominant basal melting. The model is driven by the MUN 3-D GSM (Tarasov et al. 2012; Section 2.2.6), that now includes a basal hydrology solver (Kavanagh 2012; Section 2.2.7). Together, they provide key controlling variables, such as ice thickness, sliding velocity and basal water pressure. To better isolate the sediment model behaviour's, only passive coupling between the sediment model and these driving components is currently turned on.

2.2.1 Sensitivity analysis

Any attempt to model sparsly-observed and small-scale processes, such as those included in the sediment model, is bound to include some level of idealization and parameterization with respect to their large-scale representations. This requires the use of poorly- or unconstrained parameters that can hardly lead to firm conclusions when only a single set of values is assigned to them. Rather, it is preferable to define a plausible range for each parameter (in this case, an upper, lower, and base value) and systematically generate the associated range of model outcomes. The parameters to which I assign a range are herein referred to as *sediment model parameters* and are identified by an asterisk. Their values are documented and explained in Table 2.1. The model run that uses the base value of each parameter is referred to as the *baseline run*. This approach is superior to using a single set of parameter values because it explicitly shows the bounds and the flexibility of the model, and identifies the parameters (thus the processes) to which the model is most sensitive. Furthermore, examining parametric sensitivity is an important first step toward uncertainty quantification.

2.2.2 Model numerics

The sediment model's equations are discretized by finite volumes on a staggered spherical coordinate grid spanning North America with a 1° meridional and 0.5° zonal resolution. In addition, the englacial component is solved over $N_z^\star$ vertical layers exponentially concentrated near the ice-substrate interface, resulting in a domain thickness of H_b (Table 2.1). Horizontal transport terms are temporally discretized by the explicit Euler forward scheme, whereas the implicit tri-diagonal matrix algorithm is applied to those for vertical transport. Furthermore, the transport fluxes at the interfaces are calculated from the upwind scheme, while those for vertical interfaces are computed from the power-law scheme for advection-diffusion problems (Patankar, 1980). The transport of material between grid cells and between model components conserves total sediment volume. The model is run from 120 kyr before present (BP) to present-day with asynchronous dynamic time-stepping between the components to enforce CFL conditions. Following the method of Hildes (2001; 2004), the model is initialized with present-day sediment thickness (see Figure 2.1). Based on the surficial geology map of Canada (Fulton, 1995), I define a sub-grid sediment cover factor to each surficial category (e.g. 1 for till blankets, 0.1 for till veneer). The upscaled, model-grid sediment thickness is then obtained by averaging the sediment cover factors and multiplying by a maximum initial thickness, $h_{max}^\star$. As the sediment distribution of Figure 2.1 fails to capture the intra-category variability of sediment thickness, it does not accurately represent the thickness of present-day

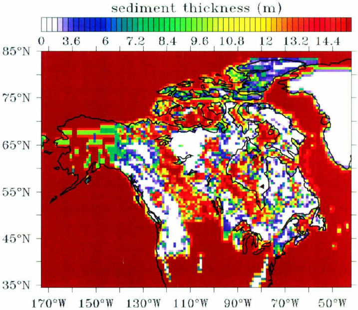

Figure 2.1: Initial sediment distribution at 120 kyr BP, based on the map of Fulton (1995). A maximum of $h^{\star}_{max}$ (base value of 15 m) is prescribed over areas of observed till blankets. Each colored square corresponds to a full grid-cell.

sediment, but merely serves as a realistic initialization map. Lastly, as transport by proglacial streams is negligible at the continental scale, it is not included in this study and I apply a no-flux boundary condition along the ice margins.

2.2.3 Subglacial erosion

Glacial abrasion and quarrying are commonly viewed as the dominant subglacial erosion mechanisms (Drewry, 1986; Glasser and Bennett, 2004). Although meltwater erosion has been hypothesized to produce significant local erosion through catastrophic outburst flood events (Shaw, 2002), it is thought to be negligible relative to abrasion and quarrying over the continental-scale (Drewry, 1986; Iverson, 2002; Cohen et al., 2006). With their own set of controlling variables, abrasion and quarrying are favoured under different glaciological conditions, but have also been shown to be controlled by lithological properties of the bed (Glasser and Bennett, 2004; Krabbendam and Glasser, 2011). The complexity of the erosion pattern over North America is a consequence of these multiple controls on glacial erosion, and it is still unclear whether this pattern can be successfully reproduced by simple empirical erosion laws (Hallet 2011; Section 2.2.3.2) , or requires a process-oriented approach, where abrasion and quarrying are modelled separately (Hildes 2001; Hildes et al. 2004; Section 2.2.3.1). Rather than adopting only one of these approaches, I favour a comparison between them and implement both in the model.

2.2.3.1 Process-oriented erosion laws

Quantitative models of glacial abrasion take the form of wear laws from material science adapted to the subglacial context (Archard, 1953; Hallet, 1979b; Boulton, 1979; Drewry, 1986; Cuffey and Alley, 1996; Hildes, 2001; Lee, 2004):

$$\dot{A} = \exp(-h_{sed}/\tilde{h}^{\star}_{sed}) \frac{k_{abr}}{HV^{\star}} \sum_{R} C_b(R) F_N(R) |v_{par}(R)| \tag{2.1}$$

where k_{abr} is the abrasion wear coefficient (0.2), $HV^{\star}$ is the Vicker hardness of the bedrock, C_b (m^{-2}) is the size-dependent basal debris concentration, F_N the contact force between the bedrock and the abrading particle, R is the particle radius, and v_{par} is the absolute velocity at which the abrading particle is dragged along the bed. The exponential factor represents shielding of bedrock by deposited sediment, where h_{sed} and $\tilde{h}^{\star}_{sed}$ are respectively the subglacial sediment thickness and a characteristic depth for the shielding effect (hereafter referred to as the shielding factor; Hildes 2001; Hildes et al. 2004; Egholm et al. 2012). Note that Equation (2.1) implicitly assumes that the abrading particle's hardness is always greater than that of the bedrock, which potentially leads to overestimating total abrasion, as soft particles cannot physically abrade a harder bedrock.

As outlined below, controlling variables $v_{par}(R)$ and $F_N(R)$ depend on the abrading particle size. Rather than choosing a single representative clast size, 10 values of R are chosen uniformly over the base-10 logarithmic scale, ranging from 1 μm to 0.1 m (i.e. clay to cobble). The product of $v_{par}(R)$ and $F_N(R)$ is weighted against the grain-size distribution, $C_b(R)$, and summed to obtain the total abrasion rate. The weights are generated by a normally-distributed particle size profile over the base-10 logarithmic scale, and scaled with the basal debris concentration by volume, as computed from the model's englacial transport component (Section 2.2.4). This calculation assumes that the debris concentration by volume is equal to the areal debris concentration in contact with the bed. Assuming a normal particle size distribution is a highly simplified approach, as these distribution are typically bi- or even poly-modal (Haldorsen, 1981; Boulton, 1978, 1979; Drewry, 1986; Hubbard and Sharp, 1995; Cook et al., 2011). This specific distribution was chosen to incorporate a wide range of particle sizes while minimizing the number of parameters required to generate it. A more detailed study could attempt to dynamically generate the particle radii distribution; this would, however, require statistical data pertaining to the specific size of debris produced by abrasion and quarrying.

With a clear dependence on bedrock hardness through the abrasion coefficient, the question of whether the abrasion law requires the incorporation of detailed lithological information arises. Such an effort is non-trivial because bedrock hardness varies within a model grid cell, prompting the use of an upscaling rule to obtain a single grid-scale value. This was done by Hildes (2001; 2004) with an area-weighting scheme. Although it is likely to affect the spatial pattern of abrasion, I treat $HV^\star$ as a uniform and constant sediment model parameter. As discussed in Section 2.3.2, however, the average abrasion depth predicted by Hallet's abrasion law (see below) is similar to that of Hildes (2001;2004)

The exact form of F_N and v_{par} differ according to the context in which they are interpreted, i.e. Hallet's or Boulton's abrasion law.

BOULTON'S MODEL

Boulton (1974; 1979) suggested that the force exerted by the abrading particle on the bedrock is proportional to the effective normal pressure, P_e, such that $F_N = A_e P_e$, where A_e is the effective area of contact. For a spherical particle of radius R in contact with a water film of thickness $h_f^\star$, this is given by $A_e = \pi(2Rh_f^\star - (h_f^\star)^2)$ (Byers et al., 2012). The friction between the clast and the bedrock causes the former to travel slower than the sliding ice (Boulton, 1979). By using Weertman's theory of basal sliding, Boulton estimated this reduced velocity as

$$v_{par}(R) = |v_s| - 2B_g^\star R \left(\frac{\mu^\star P_e A_e}{A_r}\right)^3 - \frac{P_m P_e A_e}{2L_{fus}\rho_i A_r R} \tag{2.2}$$

where v_s is the sliding velocity, $B_g^\star$ is the temperature-dependent coefficient in Glen's flow law, $\mu^\star$ is the rock-rock friction coefficient, A_r is the cross-sectional area of the particle, $\mathcal{P}_m$ is the pressure melting coefficient (7.42×10^{-8} K Pa^{-1}), L_{fus} is the latent heat of fusion (3.34×10^{-5} J kg^{-1}), and ρ_i is the ice density (910 kg m^{-3}).

HALLET'S MODEL

By recognizing that abrading particles are generally embedded in pressurized ice, Hallet (1979b; 1981) suggested that stress concentrations required for clasts to incise the bedrock remain constant under changes of normal effective pressure. His model thus asserts that effective contact forces are controlled by ice flow toward the bed rather than by the effective pressure. The normal drag exerted by the ice on the embedded clasts is expressed as (Watt, 1974):

$$F_N(R) = f_{bed}^N \frac{4\pi\eta R^3}{\tilde{R}^2 + R^2} v_n \tag{2.3}$$

where f_{bed}^N is a modification factor accounting for the presence of the bed (1.8; Byers et al. 2012), η is the effective ice viscosity, $\tilde{R}$ is the critical radius at which the drag per cross-sectional area reaches a maximum (Hallet, 1979b) and is given by $(3\eta P_m / L_{fus}\rho_i Z_r^\star)^{\frac{1}{2}}$. v_n is the normal ice velocity and in principle comprises three components: the component of the sliding velocity normal to the bed, the basal melting rate, $\dot{b}_{melt}$, and the normal component of the extensional ice velocity. Given that the relevant vertical length scale is approximately the diameter of the clasts, the extensional component is shown to be negligible (Hildes, 2001). The normal sliding component, on the other hand, is dependent on the small-scale (1-100 m) bed dip angle, e.g. positive on the stoss side of bed protrusions and negative on their lee. Ideal treatment of this term would incorporate statistical information on bed dip angles at the relevant scales. Lacking this small-scale representation, I assume that the roughness of the bed is averaged-out over the model grid-scale, yielding $v_n = \dot{b}_{melt}$. Note that i) gravitational buoyancy of the abrading particle is not included in the contact force expression because it's contribution is negligible relative to the viscous drag for particles with radius less than a few decimetres (Drewry, 1986; Iverson, 2002), and that ii) the derivation of Equation (2.3) assumes a linear ice rheology.

The particle velocity over the bed is obtained by assuming force equilibrium between the tangential drag imparted by the ice on the abrading particle and the friction with the bed, yielding

$$v_{par} = |v_s| - \frac{\mu^{\star} f^N_{bed}}{f^T_{bed}} \dot{b}_{melt} \tag{2.4}$$

where f^T_{bed} is the tangential bed modification parameter (1.7; Hildes 2001).

Although laboratory experiments favour Hallet's abrasion law (Iverson, 1990; Byers et al., 2012), questions remain whether it is appropriate in conditions of high debris concentration, where close particle interaction might induce a dependence on effective normal pressure (Hallet, 1979b; Iverson, 2002). The lack of conclusive evidence for choosing the appropriate large-scale interpretative framework, as well as the underestimated abrasion resulting from Hildes' (2001;2004) attempt to implement Hallet's law in a continental GSM (see Section 2.3.2) provides motivation for implementing and comparing Hallet's and Boulton's abrasion laws. Note that in both implementations, abrasion is neutralized when i) the particle velocity becomes negative, ii) the ice becomes cold-based, and iii) when ice reaches flotation.

QUARRYING

Quarrying is regarded as the dominant glacial erosion mechanism (Briner and Swanson, 1998; Iverson, 2002; Loso et al., 2004; Riihimaki, 2005; Cohen et al., 2006; Krabbendam and Glasser, 2011), yet a satisfying large-scale representation of it remains elusive. This is primarily due to the complex interaction between glaciological, lithological, and hydrological controlling processes and to the poor understanding of their relative contribution to large-scale quarrying rates.

Detailed theoretical analysis of stress fields in both basal ice and bedrock suggest that thin, fast flowing ice optimizes quarrying (Iverson, 1991; Hallet, 1996). Such conditions favour the formation of subglacial cavities that reduce the area of ice-bed contact and consequently enhance the stress concentration on contact points. Hildes (2001) even suggests that the absence of cavities neutralizes quarrying because it precludes the bedrock from reaching the minimum stress intensity required to propagate cracks. These analyses assume that subcritical crack growth under ice load rate-limits quarrying, thus that lithology-specific information such as minimun stress intensity (estimated from the critical stress intensity) and crack growth exponent (controls the relationship between crack propagation rates and stress intensities) are the primary lithological control on quarrying. Hildes (2001; 2004) adapts this modelling approach to the continental-scale by assuming quarrying rates proportional to subcritical crack propagation rates, which are calculated by upscaling the aforementioned lithological parameters to the model grid. Although their analysis produces realistic (but slightly underestimated) quarrying rates, field evidence suggest that this representation of quarrying is incomplete.

Indeed, Glasser et al. (1998), Duhnforth et al. (2010), and Krabbendam and Glasser (2011) show that inter- and intra-lithology variations of preglacial bedrock joint density correlates with quarrying efficiency. Furthermore, a recent study (Hooyer et al., 2012) interprets the strong correlation between the orientation of quarried surfaces and that of preglacial joints (and the associated lack of correlation with sliding direction) as evidence falsifying the assumption that subglacially-induced crack growth controls quarrying. This assumption implies that quarried surfaces should align with principal stresses imparted by flowing ice. Rather, the authors suggest that the bed should be idealized as "a series of blocks separated by discontinuous preglacial joints containing intact rock bridges". The influence of subcritical crack growth would then be restricted to the rock bridges, and thus relegated to a lesser role than in previous models.

These studies show that parameters tied to subcritical crack propagation are not necessarily the primary lithological control on quarrying rates, therefore, using them in quarrying models is difficult to justify. Rather, sub-grid information on bedrock joint density should also be included and might even be more influential. However, as pointed out in Krabbendam and Glasser (2011), joint density can vary by up to 2 orders of magnitude within a single lithology, rendering bedrock geology information impractical for incorporating this aspect in large-scale models.

The lack of spatial information on bedrock joint density forces me to assume a uniform lithological control on quarrying over the model domain. Considering the importance of subglacial cavities in the quarrying process, I scale quarrying rates with the estimated grid-scale extent of cavities. The latter is assumed proportional to the residual pressure, i.e. the difference between basal water pressure, P_w, and separation pressure, P_s, which is expressed as (Schweizer and Iken, 1992; Benn and Evans, 2010; Cuffey and Paterson, 2010):

$$P_s = P_i - \frac{\tau_b}{\pi\zeta^\star} \tag{2.5}$$

where P_i is the ice overburden pressure, τ_b is the basal shear stress (currently assumed equal to the driving stress), and $\zeta^\star$ is the basal roughness (vertical variation of bedrock features over their characteristic length).

The quarrying rate is then calculated as :

$$\dot{Q} = \exp(-h_{sed}/\tilde{h}^\star_{sed})C^\star_{quar}\left(\frac{P_w - P_s}{\tilde{P}_r}\right)^{n_p^\star} \tag{2.6}$$

where $C^\star_{quar}$ is the quarrying coefficient, $n_p^\star$ controls the influence of the residual pressure on quarrying, and $\tilde{P}_r$ is a typical value for the residual pressure (18 kPa), calculated from P_e=0.3 MPa, $\zeta^\star$=0.1, and τ_b=100 kPa (Cuffey and Paterson, 2010). Quarrying is neutralized when $P_w < P_s$. The resulting quarrying law is consistent with the accepted view of quarrying, i.e. proportional to basal water pressure and sliding speed, and inversely proportional to ice overburden pressure (Glasser and Bennett, 2004). Note, however, that this approach is novel and lacks field validation.

Treating $\zeta^\star$ as a sediment model parameter implicitly assumes that quarrying rates can be effectively estimated by an average measure of bed roughness. This is a serious simplification because topographic control of quarrying operates on a range of different scales, as suggested from the range of roche moutonnées dimensions (Benn and Evans, 2010). Nonetheless, I assume that realistic quarrying rates can be obtain by averaging topographic variation and treating roughness as a uniform sediment model parameter (Table 2.1).

There is theoretical (Iverson, 1991) and field evidence (Cohen et al., 2006) suggesting that fluctuating cavity water pressure also enhances quarrying rates. This is irrelevant at the continental-scale, however, as percolating surface water is unlikely to reach the bed and induce rapid changes in basal water pressure. Water pressure is thus likely to vary at a much lower frequency than the diurnal fluctuations observed in alpine and outlet glaciers (Benn and Evans, 2010)

Although there is general agreement on the dominance of quarrying relative to abrasion, quantitative evidence of their relative contribution to total glacial erosion is sparse. By measuring suspended sediment load and bedload in outlet streams of alpine glaciers, Loso et al. (2004) and Riihimaki (2005) estimated that quarrying is responsible for respectively 80-90% and 66% of the total sediment production. Quantitative analysis of glacial erosional landform morphology over a range of bedrock properties (Krabbendam and Glasser, 2011), however, shows that bedrock hardness and joint density dictate whether abrasion or quarrying is the dominant erosional mechanism, even under uniform glacial conditions. Thus, for soft rock with low joint density, landforms are created predominantly by abrasion, whereas quarrying dominates for hard rock with high joint density. This suggests that seeking a universal quantification of the relative strength of abrasion and quarrying might be an ill-posed problem.

2.2.3.2 Empirical erosion law

Although process-oriented erosion laws have been applied to continental-scale GSMs (Hildes, 2001; Hildes et al., 2004), there has been no attempt to evaluate whether such an approach can effectively be replaced by simple scaling relationships between erosion rates and glaciological variables, e.g. sliding velocity, ice thickness or driving stress (or some combination). Such empirical erosion laws have, however, been applied in the context of alpine and tidewater glaciers (Harbor, 1992; Herman and Braun, 2008; Kessler et al., 2008; Egholm et al., 2009, 2012), to glacial landscape evolution under ice sheets (Jamieson et al., 2005, 2008, 2010; Wilson et al., 2012), and to long-term erosion depth estimation under the Laurentide Ice Sheet (LIS; Hallet 2011). This approach has the advantage of requiring no theoretical description of small-scale subglacial processes, which minimizes the reliance on assumptions and idealizations. However, by estimating erosion from a single expression, it is implicitly assumed that all glacial erosional processes are controlled by the same grid-scale variable, thus losing the differential relative efficiency of the processes.

I follow Hallet (2011) and Pollard and Deconto (2009) and assume that glacial erosion rates scale with the product of basal shear stress (assumed equal to the driving stress) and sliding velocity (hereafter referred to as basal power):

$$\dot{E}_{emp} = \exp(-h_{sed}/\tilde{h}^{\star}_{sed}) C^{\star}_{emp} |\tau_b| |v_s| \tag{2.7}$$

This particular choice of scaling variable is supported by empirical evidence (Hallet, 2011) that allows estimation of the coefficient $C^{\star}_{emp}$ (Table 2.1). Similarly to the process-oriented laws, no erosion occurs under cold-based or floating ice.

2.2.4 Englacial transport

Observations of erratic lithologies far from their source area provide unequivocal evidence for the ability of ice sheets and glaciers to transport debris (Stravers et al., 1992; Mahaney, 1995; Larson, 2003, 2008; Benn and Evans, 2010). Debris-bearing basal ice in ice sheets and ice streams has been observed to reach thicknesses of 5 to 20 m (Drewry, 1986; Gow and Meese, 1996; Alley et al., 1997; Cook et al., 2011), representing the potential for significant debris storage and transport. Such basal layers are composed of several types of facies and are thus the product of various entrainment and mixing mechanisms. However, given the small-scale nature of englacial transport processes and their lack of large-scale theoretical representations, I employ a simplified approach in which the wide range of processes is limited to just a few. In this regard, I adapt the transport model of Hildes (2001; 2004), which consists of representing horizontal and vertical debris transport by variations in the debris concentration (by volume), $C = C(x, y, z)$:

$$\frac{\partial C}{\partial t} = -\nabla \cdot C\vec{v}_i - \frac{\partial(C\dot{V}_{net})}{\partial z} + V_{mix} \tag{2.8}$$

where $v_i = v_i(x, y, z)$ is the horizontal ice velocity. The vertical ice velocity is assumed equal to the basal melting rate and is incorporated in the net entrainment/deposition rate, $V_{net} = V_{net}(x, y)$ (see Equation 2.12). $V_{mix} = V_{mix}(x, y)$ is the heuristically defined vertical mixing rate, also discussed in the sections below. Note that C is not allowed to exceed a maximum value of $C^{\star}_{max}$; any excess concentration is redistributed to adjacent cells.

The desired outcome of this englacial transport model is to reproduce the vertical pattern of debris concentration observed in basal ice, ranging from the debris rich

(30-90%) stratified facies located near the bed, to the upper, dispersed (or clotted) facies with lower debris content (<10%) (Drewry, 1986; Knight, 1997; Waller et al., 2000; Cook et al., 2011).

2.2.4.1 Entrainment

Although basal ice entrains unconsolidated sediment by several mechanisms, I follow Egholm's (2012) and Hildes' (2001;2004) first-order assumption that regelation intrusion into the sediment is the dominant one (distinct from Weertman regelation across basal obstacles, see for example Alley et al. 1997). The theoretical basis for this process was first established by Philip (1980), who modelled ice regelating down into an array of cylinders (representing porous basal sediment). Laboratory experiments (Iverson, 1993; Iverson and Semmens, 1995) later confirmed that the intrusion rate, v_r, fitted well with the relation proposed by Philip (1980):

$$v_r = K_s \frac{P_e}{l_a} \tag{2.9}$$

where K_s is the apparent conductivity of the sediment (order of 10^{-15} m^2 Pa^{-1} s^{-1}, dependent on the sediment porosity; see Iverson and Semmens 1995, their Equations 2 and 3), and l_a is the effective thickness of the entrained sediment array. Equation (2.9) assumes that the pore-water pressure is equal to the grid-scale basal water pressure provided by the hydrology model.

In the case where v_r is greater (respectively, lower) than the deposition rate, l_a will increase (decrease) until it reaches an equilibrium thickness for which entrainment balances deposition. The dependence on l_a appears because ice must regelate around the whole array of entrained material in order to intrude further into basal sediment; thicker arrays thus provide more resistance to intrusion (Alley et al., 1997). However, this is only the case if the array is clast-supported, that is, there is close contact between embedded particles. This leads to complications when defining the effective array depth, l_a, because mixing processes dilute the entrained array and enable further regelation intrusion. l_a must therefore measure the thickness of clast-supported material rather than the total thickness of entrained debris. A satisfying definition for this was proposed by Hildes (2001) by introducing an array depth modifier:

$$l_{mod}(z) = 0.5\{\tanh[20(C(z) - C^{\star}_{crit})] + 1\} \tag{2.10}$$

This effectively represents a smoothed unit step function, and assigns large weights to concentration above $C^{\star}_{crit}$, and vice-versa. The effective array depth is then calculated as

$$l_a = \sum_{k_z} l_{mod}(k_z)\Delta z(k_z) \tag{2.11}$$

where k_z is the vertical grid cell identifier, and Δz is the grid cell thickness. The net entrainment/deposition rate, V_{net}, can now be defined as:

$$V_{net} = v_r - \frac{\dot{b}_{melt}C(z=0)}{1-\phi^{\star}} \tag{2.12}$$

where the second right-hand side term is the deposition rate, for which it is assumed that deposited sediment instantaneously acquires a porosity $\phi^{\star}$, and where $C(z=0)$ is the debris concentration by volume at the ice/bed interface. Conversely, freshly entrained debris is assumed to have a concentration of $1 - \phi^{\star}$.

As shown in Figure 2.2, the basal hydrology model predicts only a small extent highly pressurized subglacial water, which in turn yields large areas of unrealistic entrainment rates (up to 5 orders of magnitude above the basal melting rate). This prompted the addition of two ad hoc sediment model parameters designed to regulate entrainment rates: $v^\star_{max}$ imposes an upper bound on the entrainment rate and its values are chosen between the average and the maximum of $\dot{b}$, assuming that capping v_r at this level will produce more realistic net entrainment rates. $l^\star_{max}$ is the upper bound for the effective array depth above which no entrainment is allowed. The latter is justified from the theory of regelation entrainment, which predicts no entrainment after an equilibrium array thickness is reached.

2.2.4.2 Vertical mixing

Folding of basal ice has been inferred from ice cores and observed in outlet and alpine glaciers (Gow and Meese, 1996; Knight, 1997; Waller et al., 2000; Cook et al., 2011), and is argued to be the most efficient mixing mechanism (Alley et al., 1997). By assuming that folding events occur on a random basis when ice encounters bedrock obstacles, vertical mixing has been idealized as eddy-diffusion (Alley and MacAyeal, 1994). Based on simple scaling argument, the diffusion coefficient, D, is estimated as three or four orders of magnitude lower than that for thermal diffusion. We adopt this approach and express the vertical mixing term of Equation (2.8) by:

$$V_{mix} = \frac{\partial}{\partial z}\left(D\frac{\partial C}{\partial z}\right) \tag{2.13}$$

Based on the description above, it is heuristically conceivable that D should correlate with the sliding speed, and that mixing should be more pronounced near the bed, leading to the following parameterization (from Hildes 2001):

$$D = \tilde{D}^\star \left(\frac{|v_s|}{\tilde{v}_s}\right) \exp\left(\frac{-z}{\tilde{z}^\star}\right) \exp\left(\frac{-h_{sed}}{\tilde{h}^\star_{sed}}\right) \tag{2.14}$$

where $\tilde{D}^\star$ and $\tilde{z}^\star$ are scaling factors, and $\tilde{v}_s$ is a typical sliding velocity (100 m yr^{-1}). The reduction of diffusion with increasing sediment thickness assumes that there is no sliding at the ice-sediment interface, or that it does not produce considerable folding.

2.2.5 Transport by subglacial deformation

It is now generally accepted that subglacial sediment deforms and enhances ice discharge under relatively low basal shear stresses (Alley, 1991; Murray, 1997; Alley, 2000; Evans et al., 2006). It is also suggested that this process leads to large-scale ice sheet instabilities (Clark, 1994; Clark et al., 1999), although this notion has generated debate (Boulton et al., 2001; Piotrowski et al., 2001, 2002). The focus of this paper being glacial erosion and sediment transport, I include a soft-bed deformation component not for its impact on ice dynamics (which would require 2-way coupling between the MUN 3-D GSM and the sediment model), but rather for its sediment transport potential. Indeed, inferred and modelled transport distance by this process ranges from ten to several hundred kilometres (Boulton, 1996b,a; Clark and Pollard, 1998; Larson, 2003, 2008).

Calculations of the deformation flux are based on a stress-strain relationship for mass-movement in landslides (Iverson, 1985), which was first applied to subglacial material by Jenson et al. (1995), and later incorporated in several glacial system models by (Clark et al., 1996; Licciardi et al., 1998; Clark and Pollard, 1998; Tarasov and Peltier, 2004; Pollard and Deconto, 2009).

$$\tau_{sed} = c + [P_e + (\rho_s - \rho_w)gz] \tan\varphi^\star + (2D_o)^{\frac{n_s}{n_s-1}}\, \mu_o^\star \left(\frac{\partial v_{sed}}{\partial z}\right)^{1/n_s} \tag{2.15}$$

where τ_{sed} is the shear stress within the sediment, assumed equal to the driving stress,g is the gravitational acceleration (9.8 m s^{-2}), z is the vertical coordinate increasing downward from 0 at the ice-sediment interface, ρ_s and ρ_w are respectively the density of the sediment and of water (2390 kg m^{-3} and 1000 kg m^{-3}), c is the sediment cohesion and generally assumed equal to zero (Jenson et al., 1995; Cuffey and Paterson, 2010), φ is angle of internal friction of the sediment, D_o the Newtonian reference deformation rate (7.9×10^{-7} s^{-1}; Pollard and Deconto 2009), n_s the rheology exponent, and $\mu_o^\star$ the Newtonian reference viscosity. The vertical velocity profile, $v_{sed}(z)$, is obtained by integrating Equation (2.15). A second integration, from $z = 0$ to the base of the deforming layer (also called deformation depth), $z = z_d$, yields the deformation flux, Q_s. The thickness of the deforming layer is calculated from:

$$z_d = (|\tau_b| - c - P_e \tan\varphi^\star)/((\rho_s - \rho_w)g \tan\varphi^\star) \tag{2.16}$$

which is obtained from solving $v_{sed}(z) = 0$. Modelled and observed values for the deformation depth range from a few centimetres to 10 m (Alley, 1991; Jenson et al., 1995; Clark and Pollard, 1998; Alley, 2000; Boulton et al., 2001; Cuffey and Paterson, 2010).

The following assumptions are used to derive the deforming flux expression: i) sediment is thawed and saturated throughout its depth whenever the base is melting, ii) there is no vertical variation in water pressure within the sediment and, iii) the shear stress imparted by the ice is independent of z. Sediment thickness is then obtained by solving the continuity equation:

$$\frac{\partial h_{sed}}{\partial t} = -\nabla \cdot \vec{Q}_s + \dot{E} - V_{net} \tag{2.17}$$

where $\dot{E}$ is the erosion rate either from the process-oriented or the empirical erosion law.

As glaciofluvial reworking of till does not transport significant sediment volume over long, grid-scale distances, this process is not included in this thesis. The calculated sediment thickness thus represents general glacigenic deposits and does not distinguishes between primary and secondary tills.

2.2.6 Ice dynamics

The version of the MUN GSM used here includes a 3-D thermo-mechanically coupled shallow ice model, parametrized climate forcing, asynchronously coupled surface drainage solver, visco-elastic bedrock response, positive degree-day surface mass-balance (with temperature dependent degree-day melt coefficients), and detailed parameterizations for both marine and lacustrine ice calving and ice shelves. The model has been calibrated against a large set of observational geophysical constraints, including relative sea-level data and present-day rates of surface uplift. Marine limit and strand-line data have also been used to further constrain ensemble model results. Over successive calibrations the initial Eemian topography has been
adjusted to minimize discrepancy between present-day modelled (i.e. after a full glacial cycle) and observed solid-earth topography. Although a calibrated ensemble of deglacial chronologies is available, only a single, high probability set of GSM parameters is used in this study (runID nn1027 from calibration set N5bt in Tarasov et al. 2012). Details on the MUN 3D GSM and its calibration are provided in Tarasov et al. (2012) and references therein.

2.2.7 Basal hydrology

A new addition to the MUN 3-D GSM is a basal hydrology module (Kavanagh, 2012). Following the model of Flowers (Flowers, 2003), the basal water pressure is calculated from a non-linear relationship with the effective subglacial water thickness, h_w:

$$P_w = P_i \left(\frac{h_w}{h_c^\star} \right)^{\frac{7}{2}} \tag{2.18}$$

where $h_c^\star$ is the saturation thickness of the sediment. Ideally, this would be calculated from the sediment model; however, only passive coupling is currently turned on between it and the hydrology solver. $h_c^\star$ is thus treated as a sediment model parameter acting as a simple control on the magnitude of water pressure.

The effective water thickness is calculated from the continuity equation:

$$\frac{\partial h_w}{\partial t} = -\nabla \cdot \vec{Q}_w + S_w \tag{2.19}$$

where S_w is the basal mass balance (including a prescribed drainage to the aquifer). Q_w is the horizontal water flux representing drainage through cavity networks and is calculated from Darcy's law:

$$\vec{Q}_w = \frac{K_w h_w}{\rho_w g} \nabla \left(P_w + \rho_w g z_b \right) \tag{2.20}$$

where K_w is the hydraulic conductivity of the sediment (parameterized as a function of h_w) and ρ_w is the water density.

The solver also includes a down-gradient solver, adapted from the MUN 3-D GSM's surface water drainage component, to represent tunnel formation. A grid-cell is flagged as containing tunnels if one of its interface fluxes reaches a specific threshold. The water is then re-distributed by following the calculated hydraulic head gradient. Figure 2.2 shows the basal water pressure normalized against the ice overburden pressure at Last Glacial Maximum (LGM).

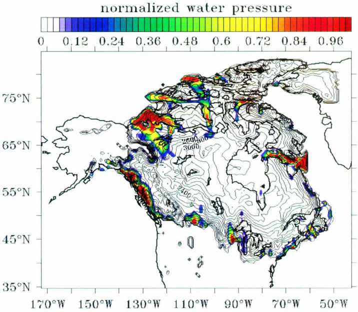

Figure 2.2: Ratio of basal water pressure and ice overburden pressure at LGM. Contours show ice thickness in metres (from runID nn1027, calibration set N5bt in Tarasov et al. 2012).

Table 2.1: Sediment model parameters. Bracketed symbols represents the abbreviations used in Figure 2.12. The range column shows lower, base, and upper values in order.

Symbol	Description	Range	Justification
$N_z^\star$ (Nz)	Number of vertical layers in the englacial component	[11, 15, 19]	Corresponds to a model domain thickness of 10.7, 15.7, and 21.4 m, respectively, and does not affect the relative grid spacing.
$C_{emp}^\star$ (Ce)	Scaling constant between basal power and erosion rate	[1.5, 8, 14]$\times 10^{-11}$ Pa^{-1}	From Hallet (2011).
$HV^\star$ (HV)	Vicker bedrock hardness	[1.5, 4, 7]$\times 10^{9}$ Pa	Range from hardness of sedimentary to metamorphic rocks (Hildes, 2001).
$\mu^\star$ (mu)	Rock-rock friction coefficient	[0.3, 0.85, 10]	Based on the compilation of Byerlee (1978), who suggest 0.85 for normal pressure above 5 MPa, but points out that a dependence on surface roughness at lower pressures can induce variations in $\mu^\star$.

Table 2.1 – Continued

Symbol	Description	Range	Justification
$R^{\star}_{mean}$ (R)	Mean of the grain-size distribution	$[10^{-4},\ 10^{-3},\ 10^{-2}]$ m	Correspond to 2.3 to -4.3 on the ϕ-scale and falls within the observed range of mean grain size in basal ice facies (Boulton, 1978, 1979; Haldorsen, 1981; Drewry, 1986; Hubbard and Sharp, 1995; Cook et al., 2011).
$h^{\star}_{f}$ (hf)	Water film thickness	$[10^{-8}, 10^{-6}, 10^{-4}]$ m	From Drewry (1986); Hubbard and Nienow (1997) and Hallet (1979a).
$B^{\star}_{g}$ (Bg)	Temperature-dependent Glen's flow law coefficient	$[24,\ 38,\ 55]\times10^{-25}$ $\mathrm{s^{-1}Pa^{-3}}$	From Cuffey and Paterson (2010)
$C^{\star}_{quar}$ (Cq)	Quarrying coefficient	$[10^{-11}, 10^{-10}, 10^{-9}]$ $\mathrm{Pa^{-1}}$	As a first order guess, I use the same range as the abrasion factor $k_{abr}/HV^{\star}$.

Table 2.1 – Continued

Symbol	**Description**	**Range**	**Justification**
$\zeta^{\star}$ (zet)	Basal roughness	[0.01, 0.1, 1]	As roches moutonnées are the remnants of quarrying events, I assume that they represent the relevant scale on which quarrying operates. The base value is thus obtained from their observed average dimensions (Krabbendam and Glasser, 2011), it also corresponds to the value used by Weertman in his theoretical analysis of basal sliding (Weertman, 1957).
$n_p^{\star}$ (np)	Quarrying law exponent controlling the influence of basal water pressure	[0.3, 0.5, 1]	Theoretical considerations (Cuffey and Paterson, 2010) suggest a value less than 1, as the presence of a critical water pressure limits the sliding velocity to a globally-controlled value that should neutralize further cavity growth even with increasing water pressures.

Table 2.1 – Continued

Symbol	Description	Range	Justification
$\tilde{h}^{\star}_{sed}$ (hs)	Shielding factor	[2, 6, 10] m	As calculated from the exponential factor in Equations 2.1, 2.6, 2.7, and 2.14, the concerned variables are reduced by half when h_{sed} is equal to 1.4, 4.1, and 6.9 m respectively.
$\varphi^{\star}$ (phi)	Angle of internal friction of subglacial sediment	[20, 22, 24]°	From Jenson et al. (1995).
$n^{\star}_{s}$ (ns)	Rheology exponent for subglacial sediment	[1.25, 1.5, 1.75]	From Jenson et al. (1995).
$\mu^{\star}_{o}$ (muo)	Newtonian reference viscosity of subglacial sediment	$[0.1, 5, 100]\times 10^{9}$ Pa s	From Jenson et al. (1995).
$\phi^{\star}$ (por)	Sediment porosity	[0.3, 0.4, 0.5]	From Clarke (2005).
$Z^{\star}_{r}$ (Zr)	Thermal resistivity of englacial debris	[0.23, 0.55, 1.1] m K W^{-1}	Ranges of thermal resistivity for limestone (Hildes, 2001). The base value is the same used in Hallet (1979b, 1981).

Table 2.1 – Continued

Symbol	Description	Range	Justification
$v^{\star}_{max}$ (vma)	Imposed upper bound on the entrainment rate	[0.02, 1.0, 8.0] m yr^{-1}	Ranges from the average $\dot{b}_{melt}$ to its maximum value, as calculated from the MUN 3-D GSM.
$C^{\star}_{max}$ (Cma)	Imposed upper bound on the sediment concentration by volume	[0.85, 0.9, 0.95]	Maximum observed englacial debris concentration (Drewry, 1986).
$\tilde{D}^{\star}$ (Dd)	Prefactor of the diffusion coefficient	$[10^{-11}, 10^{-10}, 10^{-9}]$ $\mathrm{m}^2\ \mathrm{s}^{-1}$	From Alley and MacAyeal (1994).
$\tilde{z}^{\star}$ (zd)	Scaling factor for the exponential coefficient in D	[3, 5, 7] m	Reduces diffusion by half at approximately z=[2, 3.5, 4.9] m.
$C^{\star}_{crit}$ (Cc)	Critical debris concentration for the array depth modifier	[0.3, 0.4, 0.5]	Base value is the same used in Hildes (2001).

Table 2.1 – Continued

Symbol	Description	Range	Justification
$l^{\star}_{max}$ (lma)	Cut-off entrained array thickness after which entrainment is neutralized	[2, 5, 8] m	Based on simple calculation of the equilibrium layer thickness with typical effective pressure and basal melting rate.
$h^{\star}_{max}$ (hsm)	Maximum initial sediment thickness	[10,15,20] m	Upper range of observed till blanket thickness (Alley, 1991; Hicock and Dreimanis, 1992).
$h^{\star}_{c}$ (Hc)	Sediment saturation thickness	[1, 2, 4] m	Parameter from the basal hydrology solver, used as a simple control on the magnitude of water pressure.

2.3 Results

Model results are organized along the themes of sediment transport and subglacial erosion, and are presented in the form of sediment thickness and cumulative erosion patterns. In Section 2.3.1.1, I examine the behaviour of the sediment model's transport component with a simple regional validation test. Section 2.3.1.2 describes the continental sediment distribution predicted by the model, from which the contribution of sediment deformation is assessed in Section 2.3.1.3. Erosion results using the different erosion laws are compared with each other, as well as with geological estimates of Laurentide erosion in Section 2.3.2. Results from the sensitivity analysis are presented in the final section (2.3.3), and aim to identify which sediment model parameters the model is most sensitive to and to assess the associated parametric sensitivity.

Several factors prevent a complete quantitative assessment of the sediment model's performance. Indeed, although local field estimates of glacial erosion are available at a few locations across North America (e.g. Briner and Swanson, 1998), they remain point-measurements and cannot be used as rigid constraint data until the local variability of erosion rates is better constrained (see Section 2.2.3 for discussion on the lithological controls on erosion). In this respect, only regional or continental estimates of erosion can be properly compared with the modelled erosion results. Furthermore, defining a sediment thickness metric based on the present-day distribution of sediment (Figure 2.1) is difficult to justify because: i) this thickness map was generated from the surficial geology of North America, which does not inherently contain thickness data. Assigning specific thicknesses to each surficial category, although useful for the purposes of this study, implicitly neglects the intra-category variability of sediment thickness (e.g. till blankets range from 5 to 10 m, till veneers from 0.5 to 5 m), rendering the map ill-suited for quantitative comparisons. ii) Using the present-day sediment distribution as the initialization field is only a temporary solution to counter the lack of information on preglacial sediment thickness. This simplified assumption should be replaced by a proper iterative method for inverting present-day conditions. Until this is achieved, sediment transport models cannot be quantitatively constrained by present-day conditions. Nevertheless, I attempt to determine the sensitivity of the predicted sediment distribution to initial conditions in order to use the present-day record as a qualitative target (Section 2.3.1.2).

2.3.1 Sediment transport

2.3.1.1 Application to Hudson Bay sediment

As a first test to observe the behaviour of the model's englacial and subglacial sediment transport components, I present a simple validation test based on the sediment model's baseline run and where only Hudson Bay is initially covered by sediment (uniform 20 m, see Figures 2.3 and 2.4) and for which erosion is deactivated, allowing the source of far-travelled material to be identified. This initial sediment cover roughly corresponds to present-day observations in the bay, where bottom sediment typically comprises till overlain by glaciomarine deposits and marine mud with thicknesses commonly less than 10 m, 5 m, and 5 m, respectively (Stewart and Lockhart, 2005). I assume that similar conditions existed in Hudson Bay at the onset of the Wisconsin glaciation.

Results from the model's sediment transport components cannot directly be compared with the composition of observed glacial deposits because the model lacks the ability to trace the transport paths of distinct lithological components. However, the extent of the Hudson Bay carbonate dispersal train in northern Ontario (Shilts, 1980; Hildes, 2001; Hildes et al., 2004), as well as the presence of omars (distinctive dark erratics derived from the Belcher Group in southeastern Hudson Bay) in northern United States (Prest et al., 2000) allow crude comparison with the modelled sediment transport paths and lengths. The approximate extent of these dispersal trains is shown in figure 2.5. These comparison data are by no means an exhaustive compilation of field studies pertaining to sediment dispersal by the LIS, but merely represent a minimum transport distance against which to compare the results from this validation test.

Further validation is attempted by comparing the results of this simple experiment with the conceptual model of Larson (2005; 2008), which provides an interpretative framework for explaining the dispersal pattern of Hudson Bay sediment over and beyond the Canadian Shield. This model asserts that the initial growth of the LIS over unconsolidated Hudson Bay sediment and its advance over the Canadian Shield led to the deposition of a continuous till extending from Hudson Bay to the southern LIS margin. Subsequent southward migration of the equilibrium line increased sediment fluxes over the Canadian Shield and remobilized the underlying sediment toward the margin. The lower shear stress over Hudson Bay associated with the growth of the LIS neutralized further transport from this region. According to Larson (2005; 2008), this explains the presence of far-traveled material in the southern Laurentide till sheets, the Hudson Bay carbonate dispersal train of northern Ontario, and the absence of till over the Canadian Shield.

Figures 2.3 and 2.4 show simulation results for the validation test outlined above. Englacial and subglacial sediment thickness are shown side by side for different time frames along with their corresponding volume of sediment (relative to total sediment volume). Figure 2.3a shows that the majority of this initial sediment cover was re-

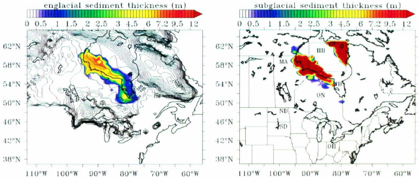

(a) 70 kyr BP, E=20% S=80%

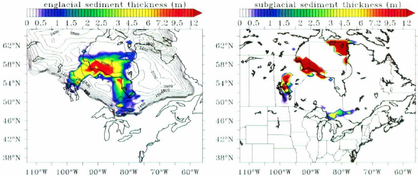

(b) 60 kyr BP, E=30% S=70%

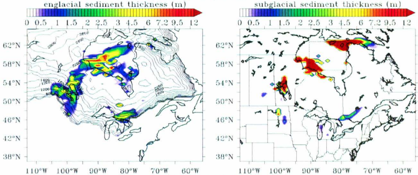

(c) 50 kyr BP, E=24% S=76%

Figure 2.3: Time slices showing englacial and subglacial sediment thickness from 70 to 50 kyr BP. Percentage of total sediment volume is shown for englacial (E) and subglacial (S) storage. Area of initial cover (uniform 20 m) is outlined by dashed lines in right panels. Contours in left panels show ice thickness in meters (from run ID nn1027, calibration set N5bt in Tarasov et al. 2012). Labels in panel (a) show Hudson Bay (HB), James Bay (JB), Manitoba (MA), Ontario (ON), North Dakota (ND), South Dakota (SD), and Ohio (OH). Variance-based color levels are used to maximize information in the 1-σ range.

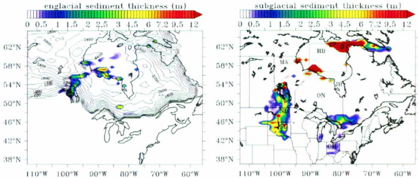

(a) 40 kyr BP, E=7% S=93%

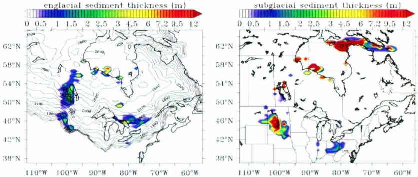

(b) 30 kyr BP, E=10% S=90%

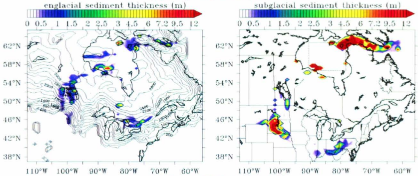

(c) 20 kyr BP, E=10% S=90%

Figure 2.4: Time slices showing englacial and subglacial sediment thickness from 40 to 20 kyr BP. Percentage of total sediment volume is shown for englacial (E) and subglacial (S) storage. Area of initial cover (uniform 20 m) is outlined by dashed lines in right panels. Contours in left panels show ice thickness in meters (from run ID nn1027, calibration set N5bt in Tarasov et al. 2012). Labels in panel (a) show Hudson Bay (HB), James Bay (JB), Manitoba (MA), Ontario (ON), North Dakota (ND), South Dakota (SD), and Ohio (OH). Variance-based color levels are used to maximize information in the 1-σ range.

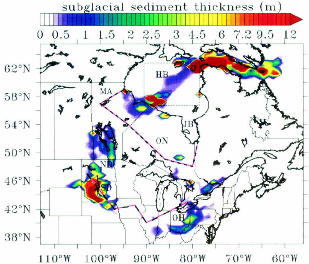

Figure 2.5: Predicted pattern of present-day sediment after 120 kyr of transport initialized with a uniform thickness in Hudson Bay (outlined by thin black dashed lines). Labels show Hudson Bay (HB), James Bay (JB), Manitoba (MA), Ontario (ON), North Dakota (ND), South Dakota (SD), and Ohio (OH). The approximate extent of the carbonate dispersal train of Northern Ontario is outlined by short, green/black dashes (Shilts, 1980; Hildes, 2001), whereas the approximate southern extent of observed omars is outlined by long, cyan/black dashes (Prest et al., 2000). Variance-based color levels are used to maximize information in the 1-σ range.

mobilized by 70 kyr BP, with active englacial transport of 20% of the total sediment volume. Subsequent transport (Figures 2.3b and 2.3c) was restricted to two predominantly southward paths: south of James Bay (JB) and in Manitoba (MA). These transport paths correlate with the sliding velocity pattern emerging from Hudson Bay (Figure 2.6), which also explains the absence of transport over western Ontario. The volume of englacial sediment peaks at 60 kyr BP, with 30% of the total sediment volume stored in the ice.

Retreat of the southern LIS margin between 50 and 40 kyr BP deposited widespread till in southern Ontario, as well as till extending roughly from central Manitoba (MA) to South Dakota (SD; Figure 2.4a). This till was partially re-incorporated in the ice during re-advance (Figures 2.4b and 2.4c), after which only the onset of deglaciation leads to major depositional events. The resulting pattern at present-day is shown in Figure 2.5.

The sediment model results of Figures 2.3 and 2.4 share some similarities with the transport model of Larson (Larson and Mooers, 2005; Larson, 2008), including the early transport of Hudson Bay sediment to the ice margin, the long-transport length of sediment deposited in northern United States, the presence of short-travelled material in northwestern Ontario, and the absence of Hudson Bay sediment between

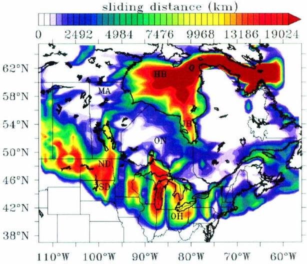

Figure 2.6: Integrated sliding velocity (absolute value) over the last glacial cycle. Variance-based color levels are used to maximize information in the 1-σ range.

these two regions. However, the widespread till deposition during the initial LIS advance predicted by his model is absent from my results. Rather, the sediment is stored englacially and does indeed extend from Hudson Bay to the margin, with major deposition events occurring only during ice margin retreat (e.g. Figure 2.4a). Furthermore, the results show minimal contribution from sediment deformation to the resulting sediment pattern (not shown), at least for its baseline run. Using the lower value of $v^{\star}_{max}$ and $\mu^{\star}_{o}$, however, reduces the amount of englacial storage and weakens the sediment, which allows more transport by deformation to occur. This specific aspect is discussed in more details in Section 2.3.1.3.

These results clearly supports that the LIS can transport sediment from Hudson Bay to its southern margin within a single glacial cycle. Although their deposition is temporally unconstrained, the presence of far-travelled omars observed south of the Great Lakes and in South Dakota (Prest et al., 2000) provides partial validation for the long-transport distances predicted by the simulations. Furthermore, Figure 2.5 shows that the model predicts short-travelled sediment in northwestern Ontario. The extent of this sediment is, however, underestimated when compared to the observed dispersal train of Hudson Bay carbonates (Shilts, 1980; Hildes, 2001; Hildes et al., 2004). Recall, however, that erosion was deactivated in this simple test. Activating erosion induces a slight increase in the extent of locally-derived sediment in Northern Ontario, but still does not yield a sediment cover as far south as the observed record. In contrast, the northern carbonate limit of 59°N predicted by this validation test is consistent with the observations.

2.3.1.2 Continental sediment distribution

Figure 2.7a shows the present-day modelled sediment thickness for the baseline run with the empirical erosion law. All processes were activated and the run was initialized with the pattern of Figure 2.1. In order to determine the sensitivity of this pattern to initial conditions, two additional model runs with different initial sediment distributions were analyzed: one was initialized with a uniform sediment cover, and the other with inverted present-day sediment thickness (i.e. $h_{sed} = h^{\star}_{max} \rightarrow h_{sed} = 0$, and vice versa). I observe that the sediment distribution of Figure 2.7a is a relatively robust model outcome. Indeed, the correlation coefficients between this sediment pattern and that obtained from the uniform and inverted initial conditions are, respectively, 0.96 and 0.88. Furthermore, the predicted pattern of Figure 2.7a remains unaffected by changes in the values of the sediment model parameters, with the majority of correlation coefficients above 0.9. Two exceptions to this general trend are the lower values of the maximum entrainment rate, $v^{\star}_{max}$, and of the sediment viscosity, $\mu^{\star}_{o}$; they yield correlation coefficients of 0.22 and 0.67, respectively. The sediment pattern corresponding to the lower value of the maximum entrainment rate is shown in Figure 2.7b. Additionally the choice of erosion law does not significantly influence the predicted sediment pattern, with correlation of 0.94 between the pattern of Figure 2.7a and that obtained from the process-oriented erosion using either Hallet's or Boulton's abrasion law.

The high correlations between the predicted sediment distribution of Figure 2.7a and that obtained from changing initial conditions, sediment model parameter values, or type of erosion provide a basis for qualitatively comparing the modelled sediment distribution (Figure 2.7a) with the observed present-day pattern of glacigenic sediment (Figure 2.1).

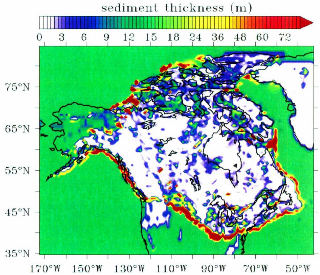

(a) Baseline run.

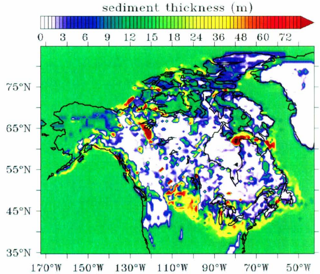

(b) Using the lower value of $v^{\star}_{max}$.

Figure 2.7: Present-day modelled sediment thickness. Using the empirical erosion law and the initialization field of figure 2.1. Variance-based color levels are used to maximize information in the 1-σ range.

Some notable features of the predicted sediment pattern of Figure 2.7a do not match the observations, including, for instance, the close to complete denudation of Hudson Bay, northern Ontario and the Rockies, as well as the absence of widespread, continuous till sheets in the Prairies and in northern United States. Rather, sediment is advected to the margin and deposited in moraines 50-300 m thick and 50-150 km wide outlining the southern, eastern, and western modelled LGM margin of the LIS. Such continuous and thick moraines are absent from the geologic record. As shown in Figure 2.7b, setting the prescribed maximum entrainment rate, $v^{\star}_{max}$, to its lower value significantly alters the predicted sediment pattern. The reduced entrainment rate increases the area of dominant basal melting and forces englacial material to be release before reaching the ice margin. This explains the 1-100 m thickness of sheet-like deposits over the southern LIS margin, which is consistent with the maximum thickness of observed glacial deposits in this region (Clark and Pollard, 1998).

2.3.1.3 Englacial vs. subglacial transport

In order to evaluate the contribution of sediment deformation to the pattern of Figure 2.7a, I present, in Figure 2.8a, the cumulative deformation predicted by the sediment model over the last glacial cycle. This pattern shows that deformation played a minor role on land, with significant transport mostly restricted to Hudson Strait, Amundsen Gulf, and coastal British Columbia. To show the maximum potential for transport by deformation calculated by the model, I present in Figure 2.8b the cumulative deformation pattern of a run initialized with a uniform sediment cover, for which entrainment was deactivated, and that used the lower value of the sediment viscosity to represent weaker sediment. The results of this model configuration highlights the potential for long-distance transport in ice streams and beneath the southern LIS, as sediment initially covering these areas have been partially, or completely advected toward the ice margin.

Alley (1991) argues that a deforming-bed model for the origin of the southern Laurentide till sheets is superior to a basal transport models because the latter requires unrealistic transport rates to explain the time-constrained deposition of the till. On the other hand, Clayton et al. (1989) suggest a melt-out origin for the till sheets, with subglacial transport restricted to a thin deforming sediment layer. The results of the baseline runs support this latter assessment, with deformation thickness generally less than a few centimetres, and an average of 0.89 m of till remobilization from deformation alone (compared to 7.3 m from englacial transport alone).

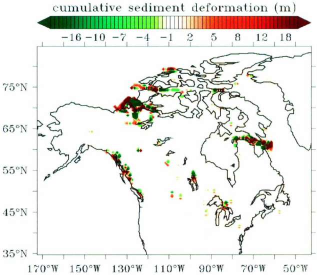

(a) Baseline run and initialized with the pattern of figure 2.1.

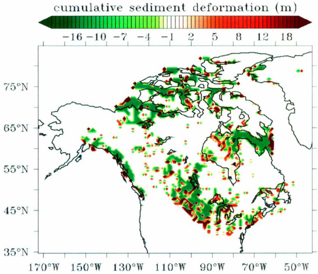

(b) Initialized with uniform sediment cover and used the lower value of $\mu_o^\star$ with deactivated entrainment and erosion.

Figure 2.8: Cumulative sediment deformation over the last glacial cycle. Positive (negative) values represent areas where accumulation (depletion) of sediment by deformation occurred. Variance-based color levels are used to maximize information in the 1-σ range.

2.3.2 Erosion

To the best of my knowledge, only three field estimates of glacial erosion over North America are appropriate to compare with and validate the erosion results from the sediment model. Given its continental extent, the estimate by Bell and Laine (1985) of 120 m of Laurentide erosion over the last 3 Myr, later revised to 80 m by Hay et al. (1989), represents the strongest constraint against which model performance may be evaluated. Average continental erosion depth was inferred by Bell and Laine (1985) by estimating the total volume of sediment produced by the LIS, both on land from the average thickness of glacigenic deposits, and in its marine sediment repositories (i.e. Canadian Arctic seas, western North Atlantic, and Gulf of Mexico) from seismic reflection data. The revision of Hay et al. (1989) was based on the alleged overestimation of the sediment volume in the Gulf of Mexico. As this geological estimate of erosion spans the entire Quaternary, it cannot be compared to the erosion depths predicted over the last glacial cycle by the sediment model. As explained below, however, this estimate is rendered compatible with the model by applying some basic assumptions regarding the total time of glacial condition over North America and the relative strength of abrasion and quarrying.

Assuming that the LIS maintained constant erosion rates throughout an estimated 2.25 Myr of glacial conditions over North America during the Quaternary[1], the estimate of Bell and Laine yields 4.2 m of erosion during the last glacial cycle averaged over the Laurentide sector (i.e. excluding contributions from the Cordilleran Ice Sheet). This value represents an upper bound, as earlier glaciations probably

---

[1] Estimated by assuming that 50 glaciations occurred during the Quaternary (Ruddiman, 2007) with 10 kyr interglacial periods, and that the onset of glacial conditions occurred at 2.75 Myr BP (Willis et al., 1999)

supported higher sedimentation rates than those of the late Pleistocene due to rapid removal of the preglacial regolith.

In addition, considering that Loso et al. (2004) inferred a minimum contribution from abrasion to total erosion of 10%, and that Iverson (2002) supports a maximum contribution of 40%, I use this range to divide the 4.2 m estimate of Bell and Laine (1985) into ranges for abrasion (0.42 - 1.68 m) and quarrying (3.78 - 2.52 m, respectively).

Two regional estimates of cumulative erosion over the last glacial cycle are also available. i) Because of its lithologically distinctive type, debris eroded from the Dubawnt Group, a Paleoproterozoic outcrop of clastic and intercalated volcanic rocks spanning 200,000 km^2 (Rainbird et al., 2003) in the District of Keewatin of western Nunavut, was identified in 800 till samples, which allowed Kaszycki and Shilts (1979) to integrate the total volume of material eroded from the outcrop. The average erosion depth was calculated to range between 6 and 20 m over the last glacial cycle. ii) Based on the ^{10}Be/^{27}Al ratio in 19 till samples located over a 100,000 km^2 region of north central Baffin Island, Staiger et al. (2006) estimated 4 to 7 m of bedrock erosion over the last glacial cycle. These two study areas are outlined by dashed boxes in Figures 2.9 and 2.10.

The cumulative erosion patterns predicted by the empirical and the process-oriented erosion laws are shown in Figures 2.9 and 2.10, respectively. The latter differentiates the abrasion patterns from Hallet's and Boulton's laws, and the quarrying pattern. All the erosion laws predict active erosion over areas of former ice stream, as well as over the southern and western margins of the LIS; however, they differ in their average erosion depths and their cumulative areas of active erosion (hereafter referred to as

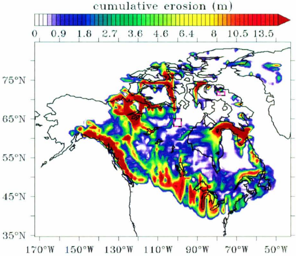

Figure 2.9: Cumulative erosion over the last glacial cycle predicted by the empirical erosion law. Average erosion depth = 3.99 m. Dashed boxes outline the Dubawnt and Beffin Island study areas where erosion depth data are available. Variance-based color levels are used to maximize information in the 1-σ range.

the erosion area), which are respectively presented in columns 1 and 3 of Table 2.2. For instance, the average abrasion depth calculated from Hallet's law is bounded by values at least one order of magnitude below the ranges for quarrying, abrasion from Boulton's law, and erosion from the empirical law. The range associated with Hallet's law is similar to the abrasion depth of 0.02 m predicted by Hildes et al. (2004). On the other hand, the quarrying pattern shows the lowest areal extent: only 57.1% of the total glaciated area compared to 90.5% for the empirical erosion law. Furthermore, all the erosion laws predict minimal erosion over the regional study areas described above, which is primarily explained by the lack of sliding over these regions predicted by the MUN 3-D GSM.

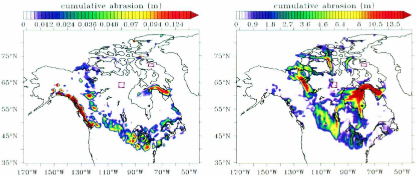

(a) Hallet's abrasion law.

(b) Boulton's abrasion law.

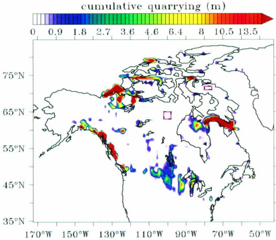

(c) Quarrying law.

Figure 2.10: Cumulative erosion over the last glacial cycle predicted by the process-oriented erosion laws. Average abrasion depth = 0.012 m (Hallet) and 1.58 m (Boulton's). Average quarrying depth = 1.38 m. Dashed boxes outline the Dubawnt and Baffin Island study areas where erosion depth data are available. Variance-based color levels are used to maximize information in the 1-σ range.

Table 2.2: Various results from the empirical and process-oriented erosion laws

Erosion law	Average erosion depth[a] (m)	Average erosion depth; LIS only[b] (m)	Erosion area[c] (%)	Dubawnt erosion (m)	Baffin erosion (m)
Abrasion (Hallet)	0.012 [7.8×10^{-4} - 0.034]	0.01 [6.6×10^{-4} - 0.028]	75.6	8.67×10^{-5}	2.34×10^{-6}
Abrasion (Boulton)	1.58 [0.26 - 15.2]	1.32 [0.21 - 12.76]	89.9	0.44	0.013
Quarrying	1.38 [0.19 - 5.47]	1.16 [0.16 - 4.6]	57.1	0.002	0.0
Empirical	3.99 [1.18 - 6.45]	3.35 [0.99 - 5.41]	90.5	0.39	0.2

[a] Averaged over the total glaciated area of North America. Brackets show the range of average erosion depths throughout the set of sensitivity runs (i.e. minimum and maximum value from Figure 2.12).

[b] Estimated by assuming a 84% contribution from the LIS to the total average erosion depths. Brackets show the range of average erosion depths throughout the set of sensitivity runs (i.e. minimum and maximum value from Figure 2.12). For comparison with the refined Bell and Laine inference of 0.42 - 1.68 m.

[c] Percentage of total glaciated area.

As the erosion depths calculated by the model apply to the whole North American ice complex, they cannot be accurately compared with the LIS-specific estimate of Bell and Laine (1985). I thus evaluate the contribution of the LIS to the total erosion pattern by assuming that erosion is proportional to ice-covered area and by estimating the areal extent of the LIS relative to the total glaciated area[2]. This simple calculation suggests that 84% of the average erosion depth calculated by the model is attributable to the Laurentide Ice Sheet. The values in column 1 of Table 2.2 are multiplied by this factor and shown in column 2, along with the similarly corrected range from the sensitivity analysis (Section 2.3.3). Comparing these ranges to the refined Bell and Laine (1985) estimate shows that abrasion from Hallet's law is underestimated by at least an order of magnitude. On the other hand, the base value for the average abrasion depth from Boulton's law falls within the Bell and Laine inference of 0.42 - 1.68 m. Note, however, that Boulton's abrasion is the least constrained of all the

---

[2] I use the value of Bell and Laine (1985) for the LIS area (~13.4 Mkm^2), and the maximum areal extent of the North American ice complex calculated by the MUN 3-D GSM (16 Mkm^2)

erosion laws with a range spanning 12.55 m. This is explained by the high sensitivity to the poorly constrained basal water film thickness parameter (see Section 2.3.3). Lastly, given their erosion depth ranges, the quarrying law and the empirical erosion law are consistent with the geological estimate.

Averaged over a 120 kyr period, the process-oriented erosion laws predict an abrasion rate of 0.1×10^{-3} mm yr^{-1} for Hallet's law, 0.013 mm yr^{-1} for Boulton's law, and a quarrying rate of 0.012 mm yr^{-1}. On the other hand, the empirical erosion law predicts an averaged rate of 0.033 mm yr^{-1}. These values (except for the abrasion rate from Hallet's model) are slightly below the lower end of the range of inferred long-term erosion rates, as reported by Koppes and Montgomery (2009) and by Fernandez et al. (2011). These studies show that modern erosion rates can exceed those of geological timescales by up to three orders of magnitude. Cases of modern erosion rates above 10 mm yr^{-1}, such as those documented by Hallet et al. (1996), thus likely result from transient periods and could not be sustained over long timescales.

2.3.3 Sensitivity analysis

The results of the sensitivity analysis are presented in Figures 2.11 and 2.12, the x-axis of which shows the sediment model parameters, presented in the order of Table 2.1, identified by their alternate abbreviations (also shown in Table 2.1). Summarizing, the englacial sediment thickness increases with the strength of erosion (controlled by the scaling coefficient of Equation 2.7, Ce) and with the sediment porosity (por; more porous sediment yields lower englacial debris concentration and increases entrainment rate through Equations 2.9 to 2.11), and is strongly reduced by the lower value of the maximum entraiment rate (vma). Abrasion from Hallet's law is most sensitive to bedrock hardness (*HV*) and maximum entrainment rate, while water film thickness (*hf*) has the most influence on Boulton's law. Quarrying is sensitive to the scaling constant (*Cq*), bed roughness (*zet*) and to the saturation thickness (*Hc*, proxy for basal water pressure, see Equation 2.18). On the other hand, erosion from the empirical law is more rigid, as only the scaling constant and the maximum entrainment rate have a significant influence on it. The sensitivity of the erosion laws to parameters related to sediment transport, such as *vma* and the sediment viscosity (*muo*), can mostly be explained by their relation to the shielding effect by subglacial sediment; parameter sets that increase englacial sediment thickness generally also increase total erosion because they allow less sediment shielding of the bedrock.

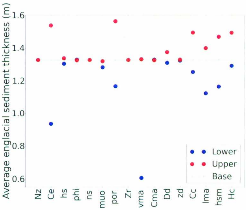

Figure 2.11: Sensitivity analysis for the englacial sediment thickness at LGM. Each point represents a model run with either the lower (blue) or the upper (red) value of a given parameter. The x-axis shows the sediment model parameters in the order presented in Table 2.1. The runs presented here used the empirical erosion law, which explains why *Ce* (abbreviation for $C^{\star}_{emp}$) replaces all the parameters related to abrasion and quarrying. Base englacial thickness=1.33 m. Some parameters have no impact and thus have confounded upper and lower points.

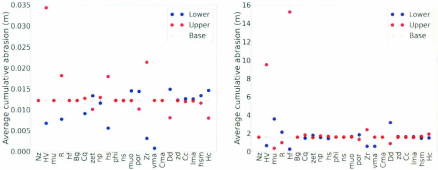

(a) Cumulative abrasion from Hallet's model. Base average abrasion depth = 0.0122 m.

(b) Cumulative abrasion from Boulton's model. Base average abrasion depth = 1.58 m.

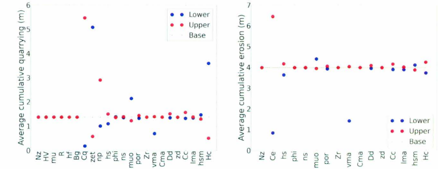

(c) Cumulative quarrying. Base average quarrying depth = 1.38 m.

(d) Cumulative erosion from the empirical erosion law. Base average erosion depth = 3.98 m.

Figure 2.12: Sensitivity analysis for the erosion laws. Each point represents a model run with either the lower (blue) or the upper (red) value of a given parameter. Results are at present-day after model runs of 120 kyr. The x-axis shows the sediment model parameters in the order presented in Table 2.1. Panel (d) was obtained with the empirical erosion law, which explains why *Ce* (abbreviation for $C^{\star}_{emp}$) replaces all the parameters related to abrasion and quarrying. Some parameters have no impact and thus have confounded upper and lower points.

In order to observe the average temporal evolution of the englacial and subglacial model components, I present, in Figure 2.13, time-series of englacial, subglacial, and eroded sediment volume normalized against the initial volume of terrestrial sediment over the last 120 kyr. I also plot the range of volumes corresponding to the sensitivity results of the scaling component, $C^{\star}_{emp}$, of the empirical erosion law. These results show that i) erosion is minimal prior to the major LIS advance at around 75 kyr BP, ii) englacial sediment volume correlates with ice volume, iii) at LGM, 20% of the total sediment volume is stored englacially, and iv) erosion generates a volume of sediment 0.5 to 1.5 times the initial sediment volume.

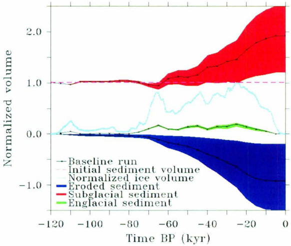

Figure 2.13: Time-series of englacial (green), subglacial (red), and eroded (blue, shown negative) volume of sediment over the last glacial cycle and normalized against the initial sediment volume (dashed pink line). The black curves are obtained from the baseline run, whereas the width of the curves corresponds to the range produced by the upper and lower value of $C^{\star}_{emp}$. In addition, ice volume (from run ID nn1027, calibration set N5bt in Tarasov et al. 2012), normalized against LGM volume, is shown in light blue for comparison against englacial sediment volume.

2.4 Discussion

I organize the following discussions along the topics of i) overestimation of sediment entrainment, ii) comparison of erosion laws, and iii) sensitivity analysis.

2.4.1 Overestimation of sediment entrainment

Although the simple validation test described in section 2.3.1.1 simulates realistic scenarios for the dispersal of Hudson Bay sediment, it fails to predict widespread sediment deposition over the Canadian Shield during the initial advance of the LIS, as hypothesized by Larson (2008; 2005) based on geomorphic evidence. I suggest that overestimated rates of regelation entrainment is sufficient to explain this shortcoming. Indeed, if the calculated entrainment rates constantly exceed basal melting rates, englacial sediment can only be deposited during ice retreat. A more realistic balance between entrainment and deposition would potentially allow englacial material to be deposited during the initial transport phase. Furthermore, two problematic aspects of the model's results can also be explained by overestimated entrainment rates:

i) As shown in Figure 2.11, the average englacial sediment thickness of the baseline run is 1.33 m. This value is, however, potentially misleading, as it is obtained by averaging over the entire glaciated area regardless of the englacial sediment content. Thus, the actual average englacial sediment thickness is higher than that presented in Figure 2.11, and, for instance, reaches above 20 m in several locations. Assuming that this net sediment thickness is distributed within the basal ice with a 5 to 25% concentration, as observed in the Byrd ice core and in exposed ice cliffs from Antarctica (Drewry, 1986), an effective thickness of 20 m extends vertically over more than 100 m in the basal ice, which exceeds the observed thickness of debris-bearing ice in ice sheets and outlet glaciers (Drewry, 1986). As suggested by the sensitivity of the average englacial sediment thickness to the maximum entrainment rate (*vma*; Figure 2.11), lower entrainment rates reduce the thickness of entrained material.

In addition, as shown in Figure 2.11, by controlling the volume of subglacial sediment available for entrainment, the scaling coefficient for the empirical erosion law (Ce) induces significant variations (0.94 - 1.57 m) in the average englacial sediment thickness (relative to the impact of other parameters). This range, however, is not proportional to the 0.9 - 6.45 m variation in the average erosion depth of the empirical erosion law (see Figure 2.12d). Thus, for model runs with minimal subglacial erosion, the ice entrains over 100% of the volume of eroded sediment, whereas less than 25% of this volume is stored englacially for runs with enhanced erosion (see Figure 2.13). This shows that the volume of sediment stored englacially is relatively independent of the volume of available subglacial material.

ii) As shown in Figure 2.7b, using the lower value of $v^{\star}_{max}$ better reproduces the observed pattern of sheet-like glacial deposits in northern United States, in contrast to the thick moraines predicted by the baseline run (Figure 2.7a) that are absent from the geologic record. This suggests that the level of englacial storage near the margin is overestimated in the baseline run and that a realistic balance between entrainment and deposition is at least partially achieved when the entrainment and basal melting rates are of the same order of magnitude.

Although capping the entrainment rate at the level of the average basal melting rate (lower value of $v^{\star}_{max}$) produces a more realistic sediment distribution, it also reduces the average erosion depths predicted by the erosion laws (see Figure 2.12). The empirical erosion law, for instance, predicts less than half of its base value when the entrainment rate is capped at the minimum, which is slightly below the 4.2 m estimate of Bell and Laine (1985). This does not, however, represent a strong drawback, as the 4.2 m estimate is an upper bound rather than a precise constraint (section 2.3.2). Nevertheless the addition of a prescribed maximum for the entrainment rate remains an ad hoc solution and hints at a serious underlying problem. Considering Equations (2.9) and (2.12), the overestimated entrainment rate can be explained by underestimated basal water pressure relative to the basal melting rate. More fundamentally, it is also possible that the entrainment law misrepresents regelation intrusion at the grid-scale level. I favour the former, as it explains two additional potential shortcomings of the sediment model:

iii) As described in Section 2.3.1.3, the contribution of sediment deformation to the pattern of glacial deposits over the southern LIS region predicted by the baseline run is minimal. As the question of whether subglacial deformation was widespread over this region has been debated and is still unresolved (Piotrowski et al., 2001, 2002), firm conclusions about the model's sediment deformation component cannot be drawn from this result. Instead, I simply emphasize that the strength of the modelled sediment deformation is flexible and can be greatly enhanced by using the lower value of the sediment viscosity (Figure 2.8b). Higher basal water pressures also induce more pervasive deformation, as Equation (2.16) predicts weaker till when the effective pressure is low.

iv) Although the total area of active erosion over North America for the last glacial cycle is not geologically constrained, it is reasonable to assume that quarrying, viewed as the dominant erosion mechanism, should have been active over more than 57% of the total LIS area. As quarrying is neutralized in zones of vanishing basal water pressure, the low area of active quarrying also suggests that the hydrology component underestimates the extent of pressurized subglacial water.

2.4.2 Comparison of erosion laws

With respect to comparing the process-oriented and the empirical erosion laws, the simulation results of Table 2.2 and the limited amount of validation data do not allow me to strongly discriminate between the two. However, given that the empirical erosion law more closely reproduces the erosion depth estimate of Bell and Laine (1985) and that it performs better than the other erosion laws over the regional study areas described in Section 2.3.2, I support that it is a viable candidate for representing large-scale subglacial erosion and should not be deemed inferior simply on the basis that it is not physically-based.

The most notable result of Table 2.2 is the low abrasion depth predicted by Hallet's law. This is either explained by underestimating the abrading particle velocities or the normal contact force. Because I observe that the particle velocities calculated from Hallet's analysis are similar to those obtained from Boulton's, I conclude that the normal ice velocity is underestimated and leads to low normal contact forces (Equation 2.3). This discrepancy probably stems from neglecting the normal component of the sliding velocity, which implicitly assumes that the impact of bed topography on abrasion averages-out over the model grid. Rather, this assumption should be replaced by a statistical representation of small-scale (1-100 m) bed dip angle variations (e.g. stoss and lee forms). Given the non-linear nature of the abrasion calculation, this addition might serve to increase the normal velocity to the required levels.

On the other hand, the base average abrasion depth predicted by Boulton's law is consistent with the 0.42 - 1.68 m range estimated in Section 2.3.2. However, this abrasion law shows high sensitivity to the basal water film thickness. Further field constraints or dynamical calculations of this variable would thus be preferable to treating it as a parameter. In addition, the high sensitivity of both abrasion laws to the bedrock hardness (Figures 2.12a and 2.12b) suggests that incorporating a lithological representation of the bed and an associated lithology-dependent abrasion law is likely to affect the cumulative abrasion pattern. This would probably reduce the estimated average abrasion depth, as cases of neutralized abrasion from soft rocks being dragged over harder beds were not accounted for in this study.

Furthermore, although the range of average quarrying depths roughly falls within the estimated range of 3.78 - 2.52 m, it remains highly sensitive to the scaling coefficient, $C^{\star}_{quar}$, and to the basal roughness, $\zeta^{\star}$. Ideal treatment of these parameters includes defining a quarrying scaling coefficient based on spatial bedrock joint density data and taking advantage of statistical information on bed roughness, as is the case for abrasion.

2.4.3 Sensitivity analysis

The results from the sensitivity analysis (Figures 2.11 and 2.12) have allowed the sediment model's parametric sensitivity to be examined. It should be emphasized, however, that the ranges obtained from this analysis, presented in Table 2.2, are not to be interpreted as proper uncertainty measures, but merely as possible scenarios that the model is able to simulate given the imposed glaciological and hydrological forcing. Rigorous uncertainty quantification would require performing an ensemble analysis with the sediment model and the basal hydrology solver, and combining them with that of the MUN 3-D GSM. Contrary to the MUN 3-D GSM, the basal hydrology solver has not been properly calibrated against field data. Given its strong impact on the processes implemented in this study, it thus represents a major source of uncertainty.

Furthermore, the lack of constraint data compatible with model results prevents a systematic refinement of the sediment model parameters to be performed. Preliminary tuning of some hydrological parameters could, however, be achieved by imposing that the average entrainment rate be of similar magnitude as the average basal melting rate, as argued above. Once implemented, this set of refined parameters should enhance model performances without requiring the use of ad hoc parameters, such as $v^{\star}_{max}$.

2.5 Summary and conclusions

The subglacial erosion and sediment transport model presented above represents a first attempt to evaluate the validity of different erosion modelling approaches and to assess the relative contribution of subglacial and englacial sediment transport in the context of continental ice sheet modelling. Based on several results presented above, including the occurrence of thick englacial sediment sequences, and the aggressive englacial transport leading to the deposition of unrealistically thick and continuous moraines, I conclude that the baseline model run overestimates sediment entrainment (and thus englacial transport). This is either explained by the large-scale misrepresentation of regelation entrainment, or by the underestimation of basal water pressure. I favour the latter because it also explains the low areal extent of active quarrying and the minimal sediment transport by deformation calculated by the baseline run. Furthermore, the fact that a realistic sediment distribution is only obtained when using the lower value of $v^{\star}_{max}$ suggests that a realistic balance between entrainment and deposition is achieved when the entrainment and basal melting rates are of the same order of magnitude.

In terms of modelled erosion, the lack of validation data precludes a proper discrimination between the different approaches implemented in this study. However, based on the realistic range of erosion depths produced by the empirical erosion law, I support that it should be considered as a valid candidate for representing large-scale subglacial erosion. On the other hand, the underestimated abrasion calculated from Hallet's law indicates that a different treatment of the normal ice velocity is needed; one where information on the small-scale bed-dip angle is incorporated to better represent the increased normal contact force on the stoss side of bedrockprotrusions. The high sensitivity of quarrying to basal roughness also suggests that a statistical representation of the bed would be appropriate. Although abrasion is shown to be highly sensitive to bedrock hardness, the lack of a lithologically-accurate representation of the bedrock does not seem to affect the total abrasion depth, as the results from Hallet's abrasion law are similar to that of Hildes et al. (2004) who included such information. Any attempt to model a geographically accurate abrasion pattern should, however, incorporate bedrock geology information as well as a lithology-dependent abrasion law.

Future work on this line of research includes applying the sediment model 2-way coupled with the MUN 3-D GSM and the basal hydrology component to timescales of multiple glacial cycles. This setup would, for instance, be appropriate to numerically evaluate the regolith hypothesis for the middle Pleistocene transition (Clark and Pollard, 1998), which has yet to be done with a 3-D GSM coupled with sediment transport and basal hydrology calculations. On the smaller scale, the coupled models could eventually be incorporated in nested modelling of ice streams to investigate the binge-purge hypothesis for Heinrich events (Alley and MacAyeal, 1994). Furthermore, examining the combined parametric sensitivity of the three coupled components is a logical next step and necessary to properly quantify model uncertainty.

This modelling effort would benefit from certain types of field data, including statistical representation of the bed roughness and bed-dip angle at the 1-100 m scale, geographically-specific bedrock joint density, and more regional estimates of cumulative erosion. Furthermore, lithology-specific estimates of the relative strength of abrasion and quarrying would provide an excellent constraint for process-oriented erosion laws.

Chapter 3

Summary

I summarize below how this thesis addresses the research questions outlined in Section 1.2, and expand, in Section 3.1, on potential future applications of the sediment model presented in Chapter 2.

- Can process-oriented erosion laws be replaced by simple empirical relationship between erosion rate and some glaciological variable?

Given that the empirical erosion law more closely reproduces the average LIS erosion depth estimated by Bell and Laine (1985) and that it performs better than the other erosion laws over the regional study areas described in Section 2.3.2, I support that it is a viable candidate for representing large-scale subglacial erosion and should not be deemed inferior on the basis that it is not physically-based. On the other hand, by having a more intricate dependance on glaciological variables, the process-oriented erosion laws allow more flexibility in the model's outcome as well as a more interpretable relationship between processes and parameters. In addition the process-oriented representations better constrain other components and processes (e.g. identification of underestimated basal water pressure, quarrying vs. abrasion). However, the similar range of average erosion depth predicted by both approaches and the limited amount of validation data precludes me from drawing firm conclusions regarding the appropriate choice of erosion law.

- When implemented in GSMs, do Hallet's and Boulton's abrasion laws produce comparable erosion patterns?

The implementation of Hallet's law presented above underestimates the average abrasion depth by at least an order of magnitude compared to the refined Bell and Laine (1985) estimate and the average abrasion depth from Boulton's law. I suggest that this is caused by neglecting the normal component of the sliding velocity and that this leads to underestimating the normal contact force of Equation (2.3). The abrasion patterns (Figure 2.10) produced by both laws are also qualitatively different, with active abrasion from Boulton's law occurring over a greater area than that of Hallet's.

- Can a large-scale quarrying law based on the extent of subglacial cavities produce realistic erosion patterns?

As shown in Table 2.2, the upper end of the range for the average quarrying depth predicted by the quarrying law (Equation 2.6) reaches the estimated 2.52 - 3.78 m derived from the estimate of Bell and Laine (1985). The areal extent of active quarrying is, however, the lowest compare to the other erosion laws and is consistent with the low extent of pressurized subglacial water predicted by the hydrology component. Lacking further validation data, the assessment of the quarrying law presented in Equation (2.6) is inconclusive.

- Which of subglacial deformation and englacial transport was the most efficient transport mechanism of the North American ice sheets?

The model's baseline run suggests minimal contribution of sediment deformation to the pattern of terrestrial glacial deposits. This is probably caused by a combination of underestimated subglacial water pressures, which leads to low deformation depths (Equation 2.16), and overestimated levels of englacial sediment storage. An overestimated sediment viscosity could also explain the lack of pervasive deformation, as the cumulative pattern of sediment deformation is highly sensitive to it (Figure 2.8b).

3.1 Future work

The potential role of subglacial processes in answering key open questions in glaciology provides motivation for further developing coupled basal process/ice sheet models. I briefly summarize two such examples below:

THE REGOLITH HYPOTHESIS FOR THE MIDDLE PLEISTOCENE TRANSITION

Spectral analysis of deep-sea oxygen isotope (δ^{18}O) records show a marked shift in the signal's dominant period of oscillation, from 41 kyr to 100 kyr at approximately 0.9 Myr before present (BP), that cannot be explained by Milankovitch theory for orbital insolation forcing. Furthermore, temporally constrained geological evidence suggesting that the late Pliocene/early Pleistocene Laurentide Ice Sheet (LIS) was as extensive as the during the late Pleistocene, coupled with δ^{18}O evidence for a volumetrically larger late Pleistocene LIS, indicates a shift from a thinner to a thicker LIS also around 0.9 Myr. This led Clark and Pollard (1998) to hypothesize that the presence of a thick, deformable regolith covering North American prior to the onset of glaciation prevented high shear stresses at the base of the LIS, thus promoting a thinner surface profile. The gradual removal of the regolith and the transition from a soft to hard bed basal condition at around 0.9 Myr potentially explains why the

LIS grew bigger during the late Pleistocene and why it responded more slowly to insolation forcing.

Clark and Pollard (1998) investigated this hypothesis with a 1-D ice sheet model coupled with a subglacial sediment deformation component based on the model of Jenson et al. (1995; discussed in Section 2.2.5). Their model reproduced several aspects of the geological record; for instance, a thin ice sheet was maintained during the earlier glaciations and advected deformable sediment toward the margins until ~1 Myr BP, when most of the base became hard-bedded. The thicker ice sheet maintained after the transition responds nonlinearly to orbital forcing with dominant 100 kyr cycles, although this relied on a fixed calving rate that was activated when the ice reached flotation.

This study highlights the potential impact of subglacial sediment deformation on glacial cycle dynamics and represents an opportunity to apply the basal process model presented in Chapter 2, although activating 2-way coupling with the MUN 3-D GSM would be necessary to reproduce the thin ice profile caused by the low basal shear stresses. The more complete set of processes included in the sediment model would allow two assumptions used by Clark and Pollard (1998) to be replaced by dynamical calculations, namely the assumption of vanishing effective pressure and that of negligible englacial transport. Furthermore, the impact of parametric sensitivity on the timing of the transition could be determined by using the sensitivity analysis presented in this thesis.

THE BINGE/PURGE MODEL FOR THE HEINRICH EVENTS

In an attempt to explain the origin of Heinrich layers in the North Atlantic sediment record, Alley and MacAyeal (1994) hypothesized that periodic surges of the Hudson Strait Ice Stream, caused either by internal processes or by external climate forcing, led to widespread entrainment of subglacial sediment and its rapid transport toward the ice margin. The increased calving rate associated with the surges generated large quantities of debris-laden icebergs that dispersed across the North Atlantic Ocean and subsequently melted out as ice rafted debris (IRD).

To evaluate this hypothesis, Alley and MacAyeal coupled a basal debris entrainment component with the low-order binge/purge model of the LIS (MacAyeal, 1993). This model asserts that the LIS undergoes long (7700 yr) periods of ice build-up (binge) when the sediment covering the floor of Hudson Bay and Hudson Strait is frozen. The gradual thickening if the ice warms the base and eventually triggers a short (750 yr) period of enhanced flow (purge) during which bed lubrification allows rapid drainage of the LIS through Hudson Strait. When the ice becomes too thin to maintain a thawed bed, the base freezes and the purge stops. After investigating different sediment entrainment mechanisms, Alley and MacAyeal concluded that only basal freeze-on by conductive cooling can generate a sufficient volume of englacial material to match the IRD discharge rates observed in the North Atlantic sediment record.

This hypothesis could be further investigated with a higher-order ice stream model coupled with a physical calving law and with the sediment model described in Chapter 2. This would involve a more complete set of subglacial processes, such as basal hydrology, transport by subglacial deformation, erosion, and sediment deposition and would allow their relative roles in generating the IRD to be identified and evaluated. The possibility of using nested modelling to assess the global impact that ice stream/bed interactions have on ice sheet dynamics also represents an interesting prospect.

In conclusion, I wish to emphasize that this line of research is still in its infancy and remains exploratory. The task of upscaling small-scale processes onto coarse, continental GSM grid is far from trivial and might require the use of empirical, or statistical laws that bear little resemblance to the small-scale representation of the relevant physical processes. Nevertheless, developing GSMs able to predict the formation of glacial erosional and depositional landforms, and in turn, using these landforms as constraint data, is an exciting prospect that represents a major advance for numerical ice sheet models.

Bibliography

Alley, R. B., 1991. Deforming-bed origin for southern laurentide till sheets? Journal of Glaciology 37 (125), 67–76.

Alley, R. B., 2000. Continuity comes first: recent progress in understanding subglacial deformation. Geological Society, London, Special Publications 176 (1), 171–179.

Alley, R. B., Cuffey, K. M., Evenson, E., Strasser, J., Lawson, D., Larson, G., 1997. How glaciers entrain and transport basal sediment: Physical constraints. Quaternary Science Reviews 16 (9), 1017–1038.

Alley, R. B., MacAyeal, D. R., 1994. Ice-rafted debris associated with binge/purge oscillations of the laurentide ice sheet. Paleoceonography 9 (4), 503–511.

Archard, J. F., 1953. Contact and rubbing of flat surfaces. Journal of Applied Physics 24 (8), 981–988.

Bell, M., Laine, E., 1985. Erosion of the Laurentide region of North America by glacial and glaciofluvial processes. Quaternary Research 23, 154–174.

Benn, D. I., Evans, D. J. A., 2010. Glaciers & Glaciation. Hodder Education, London.

Boulton, G. S., 1974. Processes and patterns of glacial erosion. In: Coates, DR (Eds.), Glacial Geomorphology. State University of New York, Binghamton,NY, pp. 41–87.

Boulton, G. S., 1978. Boulder shapes and grain-size distributions of debris as indicators of transport paths through a glacier and till genesis. Sedimentology 25 (6), 773–799.

Boulton, G. S., 1979. Processes of glacier erosion on different substrata. Journal of Glaciology 23 (89), 15–38.

Boulton, G. S., 1996a. The origin of till sequences by subglacial sediment deformation beneath mid-latitude ice sheets. Annals of Glaciology 22 (75-84).

Boulton, G. S., 1996b. Theory of glacial erosion, transport and deposition as a consequence of subglacial sediment defortnation. Journal of Glaciology 42 (140), 43–62.

Boulton, G. S., Dobbie, K. E., Zatsepin, S., 2001. Sediment deformation beneath glaciers and its coupling to the subglacial hydraulic system. Quaternary International 86 (1), 3–28.

Briner, J. P., Swanson, T. W., 1998. Using inherited cosmogenic 36Cl to constrain glacial erosion rates of the Cordilleran ice sheet. Geology 26 (1), 3–6.

Byerlee, J., 1978. Friction of rocks. Pure and Applied Geophysics Pageoph 116 (4-5), 615–626.

Byers, J., Cohen, D., Iverson, N. R., 2012. Subglacial clast/bed contact forces. Journal of Glaciology 58 (207), 89–98.

Clark, P. U., 1994. Unstable behavior of the laurentide ice sheet over deforming sediment and its implications for climate change. Quaternary Research 41 (1), 19–25.

Clark, P. U., Alley, R. B., Pollard, D., 1999. Northern hemisphere Ice-Sheet influences on global climate change. Science 286 (5442), 1104–1111.

Clark, P. U., Licciardi, J. M., MacAyeal, D. R., Jenson, J. W., 1996. Numerical reconstruction of a soft-bedded laurentide ice sheet during the last glacial maximum. Geology 24 (8), 679–682.

Clark, P. U., Pollard, D., 1998. Origin of the middle pleistocene transition by ice sheet erosion of regolith. Paleoceonography 13 (1), 1–9.

Clarke, G. K., 2005. Subglacial processes. Annual Review of Earth and Planetary Sciences 33 (1), 247–276.

Clayton, L., Mickelson, D., Attig, J. W., 1989. Evidence against pervasively deformed bed material beneath rapidly moving lobes of the southern Laurentide Ice Sheet. Sedimentary Geology 62 (2–4), 203–208.

Cohen, D., Hooyer, T. S., Iverson, N. R., Thomason, J. F., Jackson, M., 2006. Role of transient water pressure in quarrying: A subglacial experiment using acoustic emissions. Journal of Geophysical Research 111 (F3).

Cook, S. J., Swift, D. A., Graham, D. J., Midgley, N. G., 2011. Origin and significance of 'dispersed facies' basal ice: Svinafellsjokull, Iceland. Journal of Glaciology 57 (204), 710–720.

Cuffey, K. M., Alley, R. B., 1996. Is erosion by deforming subglacial sediments significant? (toward till continuity). Annals of Glaciology 22, 17–24.

Cuffey, K. M., Paterson, W. S. B., 2010. The Physics of Glaciers. Butterworth-Heinemann/Elsevier, Burlington, MA.

Drewry, D., 1986. Glacial Geologic Processes. Edward Arnold.

Duhnforth, M., Anderson, R. S., Ward, D., Stock, G. M., 2010. Bedrock fracture control of glacial erosion processes and rates. Geology 38 (5), 423–426.

Egholm, D. L., Nielsen, S. B., Pedersen, V. K., Lesemann, J., 2009. Glacial effects limiting mountain height. Nature 460 (7257), 884–887.

Egholm, D. L., Pedersen, V. K., Knudsen, M. F., Larsen, N. K., 2012. Coupling the flow of ice, water, and sediment in a glacial landscape evolution model. Geomorphology 141-142, 47–66.

Evans, D., Phillips, E., Hiemstra, J., Auton, C., 2006. Subglacial till: Formation, sedimentary characteristics and classification. Earth-Science Reviews 78 (1–2), 115–176.

Fernandez, R. A., Anderson, J. B., Wellner, J. S., Hallet, B., 2011. Timescale dependence of glacial erosion rates: A case study of Marinelli Glacier, Cordillera Darwin, southern Patagonia. Journal of Geophysical Research 116 (F1).

Flowers, G., 2003. A Multicomponent Coupled Model of Glacier Hydrology. Ph.D. thesis, University of British Columbia.

Fulton, R. J., 1995. Surficial materials of Canada. Tech. Rep. 1880A, Geological Survey of Canada.

Glasser, N. F., Bennett, M. R., 2004. Glacial erosional landforms: origins and significance for palaeoglaciology. Progress in Physical Geography 28 (1), 43–75.

Glasser, N. F., Crawford, K. R., Hambrey, M. J., Bennett, M. R., Huddart, D., 1998. Lithological and structural controls on the surface wear characteristics of glaciated metamorphic bedrock surfaces: Ossian sarsfjellet, svalbard. The Journal of Geology 106 (3), 319–330.

Gow, A. J., Meese, D. A., 1996. Nature of basal debris in the GISP2 and Byrd ice cores and its relevance to bed processes. Annals of Glaciology 22, 134–140.

Haldorsen, S., 1981. Grain-size distribution of subglacial till and its realtion to glacial scrushing and abrasion. Boreas 10 (1), 91–105.

Hallet, B., 1979a. Subglacial regelation water film. Journal of Glaciology 23 (89), 321–334.

Hallet, B., 1979b. A theoretical model of glacial abrasion. Journal of Glaciology 23 (89), 39–50.

Hallet, B., 1981. Glacial abrasion and sliding: Their dependence on the debris concentration in basal ice. Annals of Glaciology 2, 23–28.

Hallet, B., 1996. Glacial quarrying: a simple theoretical model. Annals of Glaciology 22 (1-8).

Hallet, B., 2011. Glacial erosion assessment. Tech. rep., OPG's deep geologic repository for low and intermediate level waste.

Hallet, B., Hunter, L., Bogen, J., 1996. Rates of erosion and sediment evacuation by glaciers: A review of field data and their implications. Global and Planetary Change 12 (1–4), 213–235.

Harbor, J. M., 1992. Numerical modeling of the development of U-Shaped valleys by glacial erosion. Geological Society of America Bulletin 104 (10), 1364–1375.

Hay, W. W., Shaw, C. A., Wold, C. N., 1989. Mass-balanced paleogeographic reconstructions. Geologische Rundschau 78 (1), 207–242.

Herman, F., Braun, J., 2008. Evolution of the glacial landscape of the Southern Alps of New Zealand: Insights from a glacial erosion model. Journal of Geophysical Research 113 (F2).

Hicock, S. R., Dreimanis, A., 1992. Deformation till in the Great Lakes region: implications for rapid flow along the south-central margin of the Laurentide Ice Sheet. Canadian Journal of Earth Sciences 29 (7), 1565–1579.

Hildes, D. H. D., 2001. Modelling Subglacial Erosion and Englacial Sediment Transport of the North American Ice Sheets. Ph.D. thesis, University of British Columbia.

Hildes, D. H. D., Clarke, G. K. C., Flowers, G. E., Marshall, S. J., 2004. Subglacial erosion and englacial sediment transport modelled for north american ice sheets. Quaternary Science Reviews 23, 409–430.

Hooyer, T. S., Cohen, D., Iverson, N. R., 2012. Control of glacial quarrying by bedrock joints. Geomorphology 153-154, 91–101.

Hubbard, B., Nienow, P., 1997. Alpine subglacial hydrology. Quaternary Science Reviews 16 (9), 939–955.

Hubbard, B., Sharp, M., 1995. Basal ice facies and their formation in the western alps. Arctic and Alpine Research 27 (4), 301–310.

Iverson, N. R., 1990. Laboratory simulations of glacial abrasion: Comparison with theory. Journal of Glaciology 36 (14), 304–314.

Iverson, N. R., 1991. Potential effects of subglacial water-pressure fluctuations on quarrying. Journal of Glaciology 37 (125), 27–36.

Iverson, N. R., 1993. Regelation of ice through debris at glacier beds: Implications for sediment transport. Geology 21, 559–562.

Iverson, N. R., 2002. Processes of glacial erosion. In: Menzies, J. (Ed.), Modern and Past Glacial Environment. Butterworth Heinenmann, pp. 131–145.

Iverson, N. R., Semmens, D. J., 1995. Intrusion of ice into porous media by regelation: A mechanism of sediment entrainment by glaciers. Journal of Geophysical Research 100 (B7), 219–230.

Iverson, R. M., 1985. A constitutive equation for Mass-Movement behavior. The Journal of Geology 93 (2), 143–160.

Jamieson, S. S. R., Hulton, N. R. J., Hagdorn, M., 2008. Modelling landscape evolution under ice sheets. Geomorphology 97 (1-2), 91–108.

Jamieson, S. S. R., Hulton, N. R. J., Sugden, D. E., Payne, A. J., Taylor, J., 2005. Cenozoic landscape evolution of the Lambert basin, East Antarctica: the relative role of rivers and ice sheets. Global and Planetary Change 45 (1-3), 35–49.

Jamieson, S. S. R., Sugden, D. E., Hulton, N. R. J., 2010. The evolution of the subglacial landscape of Antarctica. Earth and Planetary Science Letters 293 (1-2), 1–27.

Jenson, J. W., Clark, P. U., MacAyeal, D. R., Ho, C., Vela, J. C., 1995. Numerical modeling of advective transport of saturated deforming sediment beneath the lake michigan lobe, laurentide ice sheet. Geomorphology 14, 157–166.

Kamb, B., 1991. Rheological nonlinearity and flow instability in the deforming bed mechanism of ice stream motion. Journal of Geophysical Research 96 (B10), PP. 16,585–16,595.

Kaszycki, C., Shilts, W., 1979. Glacial erosion of the canadian shield calculation of average depths. Tech. rep., Geological Survey of Canada.

Kavanagh, M., 2012. A fast, physically-based subglacial hydrology model applied to the north american ice complex over the last glacial cycle. Master's thesis, Memorial University of Newfoundland.

Kessler, M. A., Anderson, R. S., Briner, J. P., 2008. Fjord insertion into continental margins driven by topographic steering of ice. Nature Geoscience 1 (6), 365–369.

Knight, P., 1997. The basal ice layer of glaciers and ice sheets. Quaternary Science Reviews 16, 975–993.

Koppes, M. N., Montgomery, D. R., 2009. The relative efficacy of fluvial and glacial erosion over modern to orogenic timescales. Nature Geoscience 2 (9), 644–647.

Krabbendam, M., Glasser, N. F., 2011. Glacial erosion and bedrock properties in NW Scotland: Abrasion and plucking, hardness and joint spacing. Geomorphology 130 (3-4), 374–383.

Larson, P. C., 2003. Carbonate-bearing tills on the southwestern Canadian Shield; implications for the dynamic evolution of the Laurentide ice sheet. Congress of the International Union for Quaternary Research 16, 137.

Larson, P. C., 2008. Quantification of Glacial Sediment Erosion, Entrainment, and Transport Processes and Their Implications for the Dynamic History of the Laurentide Ice Sheet. Ph.D. thesis, University of Minnesota.

Larson, P. C., Mooers, H. D., 2005. Comment on "Subglacial erosion and englacial sediment transport modeled for North American ice sheets" by D.H.D. Hildes, G.K.C. Clarke, G.E. Flowers, S.J. Marshall. Quaternary Science Reviews 24 (1-2), 233–234.

Lee, A. G. G., 2004. Experimental rock-on-rock frictional wear: Application to subglacial abrasion. Journal of Geophysical Research 109 (B9).

Licciardi, J. M., Clark, P. U., Jenson, J. W., Macayeal, D. R., 1998. Deglaciation of a soft-bedded Laurentide Ice Sheet. Quaternary Science Reviews 17 (4–5), 427–448.

Loso, M. G., Anderson, R. S., Anderson, S. P., 2004. Post–Little Ice Age record of coarse and fine clastic sedimentation in an Alaskan proglacial lake. Geology 32 (12), 1065–1068.

MacAyeal, D. R., 1993. A low-order model of the Heinrich Event Cycle. Paleoceanography 8 (6), P. 767.

Mahaney, W. C., 1995. Pleistocene and Holocene glacier thicknesses, transport histories and dynamics inferred from SEM microtextures on quartz particles. Boreas 24 (4), 293–304.

Murray, T., 1997. Assessing the paradigm shift: Deformable glacier beds. Quaternary Science Reviews 16, 995–1016.

Patankar, S. V., 1980. Numerical Heat Transfer and Fluid Flow. Hemisphere Pub. Corp. ; McGraw-Hill, Washington; New York.

Philip, J., 1980. Thermal fields during regelation. Cold Regions Science and Technology 3, 193–203.

Piotrowski, J. A., Mickelson, D. M., Tulaczyk, S., Krzyszkowski, D., Junge, F. W., 2001. Were deforming subglacial beds beneath past ice sheets really widespread? Quaternary International 86 (1), 139–150.

Piotrowski, J. A., Mickelson, D. M., Tulaczyk, S., Krzyszkowski, D., Junge, F. W., 2002. Reply to the comments by G.S. Boulton, K.E. Dobbie, S. Zatsepin on: Deforming soft beds under ice sheets: how extensive were they? Quaternary International 97–98 (0), 173–177.

Pollard, D., Deconto, R. M., 2009. A coupled Ice-Sheet/Ice-Shelf/Sediment model applied to a Marine-Margin flowline: Forced and unforced variations. In: Hambrey, M. J., Christoffersen, P., Glasser, N. F., Hubbard, B. (Eds.), Glacial Sedimentary Processes and Products. Blackwell Publishing Ltd., pp. 37–52.

Prest, V. K., Donaldson, J. A., Mooers, H. D., Division, S., Survey, G., 2000. The omar story: The role of omars in assessing glacial history of west-central north america. Geographie physique et Quaternaire 54 (3), 257–270.

Rainbird, R., Hadlari, T., Aspler, L., Donaldson, J., LeCheminant, A., Peterson, T., 2003. Sequence stratigraphy and evolution of the Paleoproterozoic intracontinental Baker Lake and Thelon basins, western Churchill Province, Nunavut, Canada. Precambrian Research 125 (1-2), 21–53.

Riihimaki, C. A., 2005. Sediment evacuation and glacial erosion rates at a small alpine glacier. Journal of Geophysical Research 110 (F3).

Ruddiman, W. F., 2007. Earth's Climate: Past and Future. W. H. Freeman.

Schweizer, J., Iken, A., 1992. The role of bed separation and friction in sliding over an undeformable bed. Journal of Glaciology 38 (128), 77–92.

Shaw, J., 2002. The meltwater hypothesis for subglacial bedforms. Quaternary International 90 (1), 5–22.

Shilts, W. W., 1980. Flow patterns in the central North American ice sheet. Nature 286 (5770), 213–218.

Staiger, J., Gosse, J., Little, E., Utting, D., Finkel, R., Johnson, J., Fastook, J., 2006. Glacial erosion and sediment dispersion from detrital cosmogenic nuclide analyses of till. Quaternary Geochronology 1 (1), 29–42.

Stewart, D., Lockhart, W., 2005. An overview of the hudson bay marine ecosystem. Tech. rep., Government of Canada, Fisheries and Oceans Canada.

Stravers, J. A., Miller, G. H., Kaufman, D. S., 1992. Late glacial ice margins and deglacial chronology for southeastern Baffin Island and Hudson Strait, eastern Canadian Arctic. Canadian Journal of Earth Sciences = Revue Canadienne des Sciences de la Terre 29 (5), 1000–1017.

Tarasov, L., Dyke, A. S., Neal, R. M., Peltier, W., 2012. A data-calibrated distribution of deglacial chronologies for the North American ice complex from glaciological modeling. Earth and Planetary Science Letters 315–316, 30–40.

Tarasov, L., Peltier, W., 2004. A geophysically constrained large ensemble analysis of the deglacial history of the North American ice-sheet complex. Quaternary Science Reviews 23 (3-4), 359–388.

Tulaczyk, S., Kamb, W. B., Engelhardt, H. F., 2000. Basal mechanics of Ice Stream B, West Antarctica 1. Till mechanics. Journal of Geophysical Research 105 (B1), PP. 463–481.

Tulley, M. J. C., 1995. Numerical Modelling of Erosion and Deposition Beneath Quaternary Ice Sheets. Ph.D. thesis, University of Cambridge.

Waller, R., Hart, J., Knight, P., 2000. The influence of tectonic deformation on facies variability in stratified debris-rich basal ice. Quaternary Science Reviews 19 (8), 775–786.

Watt, P., 1974. Inclusions in Ice. Ph.D. thesis, University of Bristol.

Weertman, J., 1957. On the sliding of glaciers. Journal of Glaciology 3 (21), 33–38.

Willis, K. J., Kleczkowski, A., Briggs, K. M., Gilligan, C. A., 1999. The role of Sub-Milankovitch climatic forcing in the initiation of the northern hemisphere glaciation. Science 285 (5427), 568–571.

Wilson, D. S., Jamieson, S. S., Barrett, P. J., Leitchenkov, G., Gohl, K., Larter, R. D., 2012. Antarctic topography at the Eocene–Oligocene boundary. Palaeogeography, Palaeoclimatology, Palaeoecology 335–336, 24–34.